Model-Based Downdraft Biomass Gasifier Operation and Design for Synthetic Gas Production

Wei-Cheng Yan[1]†, Ye Shen[1,2]†, Siming You[2], Soong Huat Sim[1], Zheng-Hong Luo[3], Yen Wah Tong[1,2], Chi-Hwa Wang[1*]

[1] *Department of Chemical and Biomolecular Engineering, National University of Singapore, 4 Engineering Drive 4, Singapore 117585*

[2]*NUS Environmental Research Institute (NERI), National University of Singapore,* #15-02, Create Tower, 1 Create Way, Singapore 138602

[3]*Department of Chemical Engineering, School of Chemistry and Chemical Engineering, Shanghai Jiao Tong University, Shanghai 200240, P. R. China*

† Authors contribute equally to this work.

*Corresponding Author. Tel: +65 65165079; Fax: +65 67791936;
Email: chewch@nus.edu.sg (C. H. Wang)

Abstract

In this study, three-phase flow model together with a thermal-equilibrium model was developed to study the operation of downdraft biomass gasifiers. Gasification experiments were conducted to obtain pyrolysis kinetics and validate the models. A good agreement was found between experiment data and model predictions, in terms of syngas composition and temperature, respectively. Kinetics based on experimental study improves the accuracy of simulation. The thermal-equilibrium model was applied to study the effects of air to biomass ratio on gas composition, LHV (lower heating value), and temperature. The 3D multiphase flow model was applied to investigate the spatial distributions of various parameters (i.e. pressure, gas velocity, temperature, and gas composition) inside the gasifier that are critical to the design of gasifier. A rough division of four gasification zones was determined based on temperature profile. It was also found that the cold gas efficiency was around 63% based on CFD (computational fluid dynamic) simulation. The temperature distributions could be used to guide the application of heat resistant materials inside the gasifier. In addition, the simulation results indicated that blockage of the gasifier has a high chance to occur at the top of reduction bell when using feedstock of high metal contents. Effects of reduction bell dimension and operation conditions on the temperature distribution and syngas production were also investigated by the 3D CFD model, which sheds light on the improvement of the design and operation of reactor. The syngas production could be enhanced by varying the size of reduction bell.

Keywords: Biomass gasification; Downdraft gasifier design; Syngas production; 3D CFD simulation.

1. Introduction

Biomass has been recognized as one of the promising renewable sources of energy, upon the gradual depletion of conventional fossil fuels (Moharamian et al., 2017; van de Kaa et al., 2017). Gasification, a thermo-chemical partial oxidation process, has great potential for biomass energy recovery, as it could convert biomass into combustible gases (i.e. syngas) that can be further converted to electricity and biochar that has a huge carbon sequestration potential (Shen et al., 2017; You et al., 2017a, Wang et al., 2017). An economically and environmentally friendly (greenhouse gas (GHG) mitigation) gasification system could be developed by balancing syngas and biochar production (You et al., 2017b). Gasifier design is a critical step to optimize the economics and green potential of a gasification system to reach cleaner energy production. A downdraft gasifier usually consists of four sequential zones, i.e. drying zone, pyrolysis zone, combustion zone, and reduction zone, respectively, among which the reduction zone is responsible for syngas production (Ravikiran et al., 2011; Ruiz et al., 2013). Currently, there are four types of commonly used gasifiers, i.e. downdraft, updraft, fluidized bed and entrained bed, respectively (Iribarren et al., 2014; Zhang et al., 2015). Downdraft gasifiers are the most widely deployed gasification technique in small-scale applications and it was reported that around 75% of gasifier manufacturers in Europe produce downdraft gasifiers (Balat and Kırtay, 2010; Klimantos et al., 2009; Ong et al., 2015; Patra and Sheth, 2015; Rollinson and Karmakar, 2015).

Conventional experiment-based gasifier designing methods are generally time-consuming and costly, hindering the quick update of gasification technology. For industrial-scale gasification systems, the experiment-based methods are exceptionally undesirable in terms of safety and cost (Li et al., 2004). In this case, modeling-based methods (i.e. mathematical models and computational fluid dynamics (CFD) simulation) provide alternative ways to the designing and optimization of gasification systems.

Various mathematical models have been developed to describe gasification systems, and these models could be generally classified into thermal-equilibrium models and one-dimensional (1D) kinetic models, respectively (A list of selected existing modeling studies is given by **Table 1**.). However, most of the reported thermal-equilibrium models for downdraft gasifiers have either considered the reduction zone only(Sharma, 2008a) or

modeled the four zones as a single lumped zone (Jarungthammachote and Dutta, 2007; Melgar et al., 2007). Similarly, most of the 1D models (Ephraim et al., 2015; Gao and Li, 2008) considered one or two of the four zones only. It is an inherent shortcoming of thermal-equilibrium and 1 D models for being unable to differentiate the four gasification zones unless initial defined (Ong et al., 2015). As a result, it is necessary to resort to more sophisticated models to develop the model-based ability to differentiate the gasification zones. Also, thermal-equilibrium models and 1 D models fail to provide detailed inside information of the reactors. To overcome these barriers, recently, CFD simulation has been adopted to study the operation of gasification systems despite that most of existing CFD simulation focused on entertained bed or fluidized bed gasifiers (Marklund et al., 2007; Papadikis et al., 2009; Xue et al., 2011). For limited CFD simulation of downdraft gasifiers, significant simplification such as adopting 2D simplified configuration instead of 3Dhas been applied by some existing studies (e.g., Gerun et al. (2008) and Wu et al. (2013)). This could potentially affect the accuracy and practical application of those models. Specially, Gerun and colleagues (Gerun et al., 2008) developed a simplified 2D CFD model and modeled the oxidation zone of a downdraft gasifier only. Wu and colleagues. (Wu et al., 2013) employed 2D slab geometry in their simulation model, which obviously does not reflect the actual geometrical structure of most commonly used downdraft gasifiers whose slabs are 3D asymmetric. Furthermore, their 2D CFD model provided limited information about the interior of gasifiers. Hence, it is necessary to develop a 3D CFD model considering all the four zones and 3D asymmetric geometry of downdraft gasifiers to improve the existing CFD-based design capability (Ahmed et al., 2012)

To improve the existing models and extend their application to the designing of downdraft gasifiers, this work developed a 3D CFD model together with a thermal-equilibrium model for downdraft gasifiers. The combined use of thermal-equilibrium and 3D CFD models could serve as an effective tool for designing gasifiers. Compared to the 3D CFD model, the thermal-equilibrium model could provide a more efficient way of analyzing the producer gas composition. Based on the thermal-equilibrium model, the highest gasification efficiency achievable for a given type of feedstock could be estimated, which guides the selection of feedstock. Hence, the thermal-equilibrium model

could be used to design the operating conditions towards optimal gas output in a steady state. However, the equilibrium-state assumption disables the thermal-equilibrium model to provide any transient information about the operation of gasifiers and the physicochemical phenomena inside gasifiers. In this case, the 3D CFD model could be used to compensate the shortcomings of the thermal-equilibrium model. Especially, the effect of gasifier geometry on the gasification process could be understood based on the 3D CFD model by correlating the fluid behavior, heat and mass transfer with chemical reactions. In addition, the effect of gasifier geometry provides straightforward information for gasifier design.

This work aims (1) to develop a comprehensive gasifier design platform that utilizes the efficiency of thermal-equilibrium model and the delicacy of 3D CFD model, and (2) to shed light onto the design of downdraft gasifier based on the platform. Specially, the thermal-equilibrium model was built based on elemental mass balance and energy balance. A three-phase flow model was proposed to simulate wood, char and gas phases for 3D CFD simulation. Gasification experiments based on a commercially available gasifier were conducted to validate the developed models, in terms of the temperature and syngas composition in the gasifier. To further improve the accuracy of 3D CFD model, pyrolysis kinetics were studied experimentally. The thermal-equilibrium model was applied to study the effects of air to biomass ratio on gas composition, LHV (lower heating value) and temperature, and the 3D CFD model was applied to study the distributions of various parameters (i.e. pressure, gas velocity, temperature, gas composition) inside the gasifier. Effects of reduction bell dimension and operation environment were also investigated by the 3D model to guide the improvement of gasifier operation and design.

2. Computational Models

2.1 Thermal-equilibrium model

A schematic of thermal-equilibrium model is shown in **Figure 1**. The thermal-equilibrium model assumes that (Jarungthammachote and Dutta, 2007; Melgar et al.,

2007; Sharma, 2008a, b): (a) the residence time of biomass in the gasifier is long enough to achieve chemical equilibrium; (b) the final gas in the gasifier is comprised of H_2, CO, CO_2, H_2O, CH_4 and N_2; (c) the inside of the gasifier has uniform atmospheric pressure and temperature; (d) ash content is inert throughout the process. Air is introduced into the gasifier with the temperature of T_{air} after preheating. Elemental mass balance and energy balance were introduced into the thermal-equilibrium model to predict the gas composition and the temperature of the gasifier, respectively.

Raw biomass materials can be expressed as $CH_xO_yN_z$ with

$$x = \frac{HM_c}{CM_H},\ y = \frac{OM_c}{CM_o},\ z = \frac{NM_c}{CM_N} \quad (1\text{-}3)$$

C, H, N and O are the mass fractions, while M_C, M_H, M_N and M_C are the molecular weights of carbon, hydrogen, nitrogen and oxygen in the feedstock, respectively. The generalized reaction (Jarungthammachote and Dutta, 2007; Melgar et al., 2007) is

$$CH_xO_yN_z + m(O_2 + 3.76N_2) = n_{H_2}H_2 + n_{CO}CO + n_{CO_2}CO_2 + n_{H_2O}H_2O + n_{CH_4}CH_4 + n_{\text{tar}}Tar + (1\text{-}\alpha_c)\,Char + \left(\frac{z}{2} + 3.76m\right)N_2 \quad (4)$$

Carbon balance leads to

$$n_{CO} + n_{CO_2} + n_{CH_4} - 1 = 0 \quad (5)$$

Hydrogen balance leads to

$$2n_{H_2} + 2n_{H_2O} + 4n_{CH_4} - x = 0 \quad (6)$$

Oxygen balance leads to

$$n_{CO} + 2n_{CO_2} + n_{H_2O} - 2m - y = 0 \quad (7)$$

where m is mole ratio between air and the feedstock. n_i is the mole of composition i in the final product.

Independent reactions in the reduction zone were used to describe the equilibrium balance among producer gas species. The water–gas shift reaction is $CO + H_2O = CO_2 + H_2$ with the equilibrium constant of

$$K_1 = \frac{n_{CO_2} \times n_{H_2}}{n_{CO} \times n_{H_2 o}} \quad (8)$$

where K_1 is evaluated based on Pedroso et al.(2008):

$$K_1 = e^{\frac{4276}{T} - 3.961} \quad (9)$$

The methane reaction is $C + 2H_2 = CH_4$ with the equilibrium constant of

$$K_2 = \frac{n_{CH_4} \times n_{total}}{n_{H_2} \times n_{H_2}} \quad (10)$$

where K_2 is evaluated based on the relationship given by Zainal et al. (2001):

$$\ln(K_2) = \frac{7082.842}{T} - 6.567 \times \ln(T) + \frac{(7.467 \times 10^{-3}) \times T}{2} - \frac{2.167 \times 10^{-6}}{6} \times T^2 + \frac{0.702 \times 10^5}{2 \times T^2} + 32.541 \quad (11)$$

Tar, the unwanted by-product during gasification could be predicted using the following correlation, as suggested by Sadaka (Sadaka et al., 2002), where W_{tar} is the weight percentage of tar in total products.

$$W_{tar} = 35.98 e^{-0.00298T} \quad (12)$$

Carbon conversion factor could be expressed by a function of temperature and equivalence ratio (Lim et al., 2014):

$$\alpha_c = 0.901 + 0.439 \times (1 - e^{-ER + 0.0003T}) \quad (13)$$

The heat balance equation is

$$H^0_{f,woodchips} + \left(mH^0_{f,O_2} + 3.76mH^0_{f,N_2} + Q_{air}\right) = \sum n_j \left(H^0_{f,j} + \int_{298}^{T} c_{p,j} dT\right) + (3.76m + z/2)(H^0_{f,N_2} + \int_{298}^{T} c_{p,N_2} dT) \quad (14)$$

with

$$Q_{air} = m \int_{298}^{T_{air}} C_{p,O_2} dT + 3.76m \int_{298}^{T_{air}} C_{p,N_2} dT \quad (15)$$

$$C_p = a + bT + cT^2 + dT^3 \quad (16)$$

where n_j represents n_{CO}, n_{CO_2}, n_{H_2O} n_{CH_4} and n_{H_2}.

The formation heat of solid fuel can be expressed as

$$H^0_{f,woodchips} = HHV_{woodchips} + \Sigma n_k H^0_{f,k} \quad (17)$$

where n_k represents n_{CO_2}, n_{H_2O}, and n_{NO_2}.

The HHV of solid fuel was estimated based on the relationship derived by Channiwala

and Colleague (Channiwala and Parikh, 2002),

$$HHV = 0.3491C + 1.1783H + 0.1005S - 0.1034O - 0.0151N \quad (18)$$

2.2 3D CFD model

In the 3D CFD model, the Eulerian-Eulerian three-phase flow model was employed to describe the flow behavior of each phase, with the reacting gas flow as the primary phase and both the biomass and char as the secondary phase. The species transport model was used to describe the species conservation in the gas phase and homogeneous reactions.

2.2.1 Governing equations

Mass balance for the q^{th} phase is computed by continuity equations:

$$\frac{\partial}{\partial t}\left(\alpha_q \rho_q\right) + \nabla \bullet \left(\alpha_q \rho_q \vec{v}_q\right) = \sum_{p=1}^{N}\left(\dot{m}_{pq} - \dot{m}_{qp}\right) \quad (19)$$

where $\vec{v}_q$ is the velocity of phase q and $\dot{m}_{pq}$ ($\dot{m}_{qp}$) is the mass transfer from the phase p (q) to phase q (p). A multi-fluid granular model is used to describe the flow behavior of a solid-fluid mixture. The conservation of momentum for a fluid phase (i.e. gas phase) is

$$\frac{\partial}{\partial t}\left(\alpha_g \rho_g \vec{v}_g\right) + \nabla \bullet \left(\alpha_g \rho_g \vec{v}_g \vec{v}_g\right) = -\alpha_g \nabla P + \nabla \bullet \bar{\bar{\tau}}_g + \alpha_g \rho_g \vec{g} + \sum_{p=1}^{N}\left(K_{pg}\left(\vec{v}_p - \vec{v}_g\right) + \dot{m}_{pg}\vec{v}_{pg} - \dot{m}_{gp}\vec{v}_{gp}\right) \quad (20)$$

where K_{pg} is the momentum exchange coefficient between the gas phases g and p.

The conservation of momentum for a solid phase (i.e. char or biomass) is

$$\frac{\partial}{\partial t}\left(\alpha_S \rho_s \vec{v}_s\right) + \nabla \bullet \left(\alpha_S \rho_s \vec{v}_s \vec{v}_s\right) = -\alpha_S \nabla P - \nabla P_s + \nabla \bullet \bar{\bar{\tau}}_s + \alpha_S \rho_s \vec{g} + \sum_{p=1}^{N}\left(K_{ps}\left(\vec{v}_p - \vec{v}_s\right) + \dot{m}_{ps}\vec{v}_{ps} - \dot{m}_{sp}\vec{v}_{sp}\right) \quad (21)$$

where K_{ps} is the momentum exchange coefficient between the solid phases s and p.

The energy equation for the q^{th} phase can be expressed as

$$\frac{\partial}{\partial t}\left(\alpha_q \rho_q h_q\right) + \nabla \bullet \left(\alpha_q \rho_q \vec{v}_q h_q\right) = \alpha_q \frac{\partial P_q}{\partial t} + \bar{\bar{\tau}}_q : \nabla \vec{v}_q - \nabla \bullet \vec{q}_q + S_q + \sum_{p=1}^{N}\left(Q_{pq} + \dot{m}_{pq} h_{pq} - \dot{m}_{qp} h_{qp}\right) \quad (22)$$

where h_q, $\vec{q}_q$, S_q, Q_{pq} and h_{pq} are the specific enthalpy of the q^{th} phase, the heat flux, the source term which includes the heat loss at wall, the intensity of heat exchange between the p^{th} and q^{th} phases and the interphase enthalpy, respectively.

$$Q_{pq} = h'_{pq}\left(T_p - T_q\right) \quad (23)$$

where h'_{pq} is the volumetric heat transfer coefficient between the phases p and q, and it is related to the Nusselt number of phase p, Nu_p as

$$h'_{pq} = \frac{6\kappa_q \alpha_p \alpha_q Nu_p}{d_p^2} \quad (24)$$

where κ_q is the thermal conductivity of the q^{th} phase. The Nusselt number correlation by Gunn (Gunn, 1978) is expressed as the following:

$$Nu_p = \left(7 - 10a_f + 5a_f^2\right)\left(1 + 0.7Re_s^{0.2}Pr^{\frac{1}{3}}\right) + \left(1.33 - 2.4a_f + 1.2a_f^2\right)Re_s^{0.7}Pr^{1/3} \quad (25)$$

where a_f is the porosity of fluidized bed; Pr is the Prandtl number; Re_s is the Reynolds number.

Species transport equations for the species in gas phase is

$$\frac{\partial}{\partial t}\left(\alpha_g \rho_g Y_i\right) + \nabla \bullet \left(\alpha_g \rho_g Y_i \vec{v}_g\right) = -\nabla \bullet \rho_g D_i \nabla Y_i + S_i \quad (26)$$

The interphase momentum exchange K_{ps} between the gas (when $p = g$) and solid phases is described by the Gidaspow drag law (Gidaspow, 1994) as

$$K_{gs} = \frac{3}{4} C_D \frac{\alpha_s \alpha_g \rho_g \left|\overrightarrow{v_s} - \overrightarrow{v_g}\right|}{d_s} \alpha_g^{-2.65} \ (\alpha_g > 0.8)\,, \quad (27)$$

where

$$C_D = \frac{24}{\alpha_g Re_s}\left[1 + \left(\frac{3}{20}\alpha_g Re_s\right)^{0.687}\right] \quad (28)$$

$$Re_s = \frac{\rho_g d_s |\vec{v}_s - \vec{v}_g|}{\mu_g}, \quad \text{and,} \tag{29}$$

$$K_{gs} = 150 \frac{\alpha_s (1-\alpha_g)\mu_g}{\alpha_g d_s^2} + \frac{7}{4} \frac{\alpha_s \rho_g |\overrightarrow{v_s} - \overrightarrow{v_g}|}{d_s} (\alpha_g \leq 0.8). \tag{30}$$

The solid-solid exchange coefficient K_{ps} between the p^{th} solid phase and s^{th} solid phase is calculated by Syamlal (1987):

$$K_{ps} = \frac{3(1+e_{ps})\alpha_s \alpha_p \rho_s \rho_p (d_p + d_s)^2 g_{0,ps}}{4(\rho_s d_s^3 + \rho_p d_p^3)} \left| \overrightarrow{v_p} - \overrightarrow{v_s} \right| \tag{31}$$

where e_{ps} is the coefficient of restitution, $d_p$is the particle diameter of solid p, and $g_{0,ps}$ is the radial distribution coefficient.

2.2.2 Reaction kinetics

In a downdraft gasifier, the drying zone is located at the top of the reactor where the biomass is being fed. The drying-required energy (heat) is transferred from the zones at the bottom of the reactor.

$$\text{Moist Biomass} \xrightarrow{\text{heat}} \text{Dried Biomass} + H_2O \tag{32}$$

The dried biomass (8.22 wt% water for the experiment) was considered in the simulation. The chemical reactions occurring inside the gasifier were divided into two categories, namely, the homogeneous reactions of gas phase and heterogeneous reactions among different phases. The corresponding chemical reactions and kinetics were summarized in **Tables 2-3**.

2.2.3 Geometry and mesh

The geometry of the gasifier corresponding to the one used in the following validation experiments is shown in **Figure 2(a)**. Five nozzles located around the bottom of the gasifier serve as the air inlet and none of the nozzles is facing directly opposite to one another. The biomass inlet is located at the top of the gasifier. The syngas outlet is at the bottom of the reduction bell. The 3D geometry (**Figure 2(a)**) and corresponding mesh of this downdraft gasifier were created using ANSYS GAMBIT (**Figure 2(b)**). A denser mesh was used for the region around air nozzles to ensure accuracy, considering the geometric complexity of this region. Grid independence analysis was conducted and it

was found that a total amount of 55151 grid number was able to ensure the convergence and accuracy of the simulation while saving the computational cost.

2.2.4 Simulation strategy

The simulation was run on FLUENT 14.5 (ANSYS, US). Eulerian-Eulerian three-phase gas-solid model was employed to describe the flow behavior of each phase with the reacting flow as the primary phase and both the biomass and char as the secondary phase. Woodchips (corresponding to the following validation experiments) are used as the feedstock and has a density of 602 kg/m^3 and an equivalent particle diameter of 0.04 m. The char produced in the gasification process has a density of 2000 kg/m^3 and an equivalent particle diameter of 0.02 m. The packed density of feedstock is 60% with respect to the bed volume in the gasifier. The operating pressure for the gasifier was set at 1 atm and the temperature of the inlet air was set at 500 K. More details can be found in **Table 4**. The physical properties of the biomass used by simulation are shown in **Table 5**.

It was assumed that the gas phase was fully turbulent within the packed bed and the effect of molecular viscosity was negligible. Hence, a standard $k-\varepsilon$ model was used for the gas phase. Finite-rate/Eddy-dissipation model was used to account for both the Arrhenius and Eddy-dissipation, and calculate the net reaction rates of the species. The bottom portion of the gasifier near the air nozzles was patched at 1000 K to ignite the combustion process. The time step was 10^{-7} seconds and the maximun iteration rate was 20 per time step. To avoid the convergence problem and reduce computational cost, a multi-stages calculation method was used for the 3D CFD model(Chen et al., 2011). The CFD simulation flow chart is shown by **Figure 3**. In the first stage, only the flow equations were solved. After the flow field was fully developed, the second stage began and all the individual species, turbulence and volume fraction equations were added to the existing calculation. Once the residual value falls into the converge criteria, the energy equation was added into the total calculation, which was the third stage. The time-avergaged results were selected for analysis, after the simulated system become stable, namely, the outlet composition of syngas and temperature hardly changed or fluctuated around a certain value.

3. Experiments

3.1 Pilot-scale gasification

A schematic diagram of the gasification system (ALL POWER LAB, Berkeley, California, USA) mainly consisting of a 10 kW downdraft fix-bed gasifier is shown by **Figure 4**. The biomass (woodchips) was firstly introduced into the hopper and then entered the gasifier after passing through the auger controlled by a level switch at the reactor lid. The biomass filled the reactor through the four stages of gasification, i.e. drying, pyrolysis, combustion, and reduction, respectively. The air was introduced into the gasifier through 5 air nozzles. The pipelines containing air got heated up by the exiting producer gas in the interlayer. The exiting producer gas passed through a cyclone for removing large particles, followed by the passing-through of a gas filter and gas drive system, subsequently. In the end, the syngas with high fuel efficiency was fed into an engine to generate electricity.

During the operation, two thermocouples were installed in the combustion and reduction zones, respectively, to measure the temperature inside the gasifier. Upon steady state, the temperature readings from the two thermocouples reached 800°C and 650°C respectively. The out-wall temperature of the reactor at three different height locations was also measured to study the heat loss of the system with a K-type thermocouple as shown in **Figure 4**. Temperature and gas composition were analyzed based on an average of 10-min measurement. Detailed experimental procedures and results could be found in our previous study (Ong et al., 2015).

At the very beginning of the experiments, a series of elemental analysis test was conducted to determine the chemical composition of the woodchips. The biomass capacity of the gasifier is 10 kg/h, while only milligrams of woodchip samples are used for elemental analysis. Hence, a standard sampling method, the cone and quartering method, was adopted to collect representative woodchip samples for elemental analysis (**Figure 5**). A bag of woodchips was firstly mixed and poured into a cone-shaped heap on a flat plane (**Figure 5(a)).** The heap was then divided into four identical volumes (**Figure 5(b)**). The two quarters sit opposite to each other were discarded, while the other two

were mixed as a new heap (**Figure 5(c)**). The process was repeated twice to further reduce the sample volume. In the end, three groups were randomly picked from each quarter for elemental analysis. As shown in **Table 5**, for the carbon and hydrogen content, the intra-and inter-group differences were minor, compared with the average value, showing that the reliability of the cone and quartering method.

3.2 Experimental kinetic study of woodchip pyrolysis

Different kinds of woodchips usually have various pyrolysis kinetics, which could cause differences in gas production. Thus, to further improve the accuracy of CFD simulation model, the kinetics of woodchip pyrolysis (R5) was obtained experimentally. The new kinetics was also employed in CFD simulation to compare with the case where kinetics data came from literature.

3.2.1 Reaction rate

The reaction rate of woodchip pyrolysis was studied by thermogravimetric analysis (TGA) using a Shimadzu DTG-60AH thermal analyzer at heating rate of 10, 20, 30, and 40 °C/min, respectively. For each group, woodchips were heated up to 900 °C. Similar as R5, a first order reaction rate expression was assumed as following (Mohammed et al., 2017):

$$\frac{d\alpha}{dt} = Ae^{-\frac{E}{RT}}(1-\alpha) \tag{33}$$

where α, A and E represents for conversion rate, pre-exponential factor and activation energy.

Conversion rate α, could be calculated as

$$\alpha = \frac{m_0 - m_t}{m_0 - m_f} \tag{34}$$

where m_t, m_0 and m_f stand for transient mass, initial mass and final mass of the feedstock.

According to Kissinger Method (Wang et al., 2016), under condition of maximum reaction rate, the following expression could be reached, where T_m is the corresponding temperature at this moment.

$$\frac{d^2\alpha}{dt^2} = \frac{d\alpha}{dt}\left(\frac{\beta E}{RT_m{}^2} - Ae^{-\frac{E}{RT_m}}\right) = 0 \quad (35)$$

After rearranging, the correlation between heating rate β and T_m is obtained.

$$\ln\left(\frac{\beta}{T_m^2}\right) = \ln\left(\frac{AR}{E}\right) - \frac{E}{R}\frac{1}{T_m} \quad (36)$$

By plotting $\ln\left(\frac{\beta}{T_m^2}\right)$ with $\frac{1}{T_m}$, from the slope and intercept, E and A could be reached.

3.2.2 Gas composition

The gas composition from woodchip pyrolysis was determined in a lab-scale fixed bed gasifier, as shown in **Figure 6**. Feedstock was put in the stainless steel reactor (1 m long) surrounded by a furnace prior to experiment. During experimental analysis, the reactor was heated up to 900 °C. Nitrogen, controlled by mass flow controller was used as purging gas. After pyrolysis reaction, tar trapping system and washer were set to capture tar. In the end, gas samples were collected by gas bags, which were further analyzed through gas chromatography, while char remained in the reactor. Tar component was calculated based on mass balance.

4. Results

4.1 Experimental kinetic study of woodchips pyrolysis

4.1.1 Reaction rate

As shown in **Figure 7(a)**, the temperature for maximum reaction rate, T_m increases with heating rate β. After plotting $\ln\left(\frac{\beta}{T_m^2}\right)$ with $\frac{1}{T_m}$, pre-exponential factor A and activation energy E were obtained as 1.3×10^5 and 87.4 kJ/mol with coefficient of determination of 0.98.

4.1.2 Gas composition

Figure 7(b) shows transit gas composition during pyrolysis. In the earlier stage (0-10 mins), temperature of woodchips increased gradually. When it reach certain value, pyrolysis took place immediately, as describe at around 10 mins in the figure. After that, fast decomposition reaction could be observed from 10-20 mins. This implied that pyrolysis plays a crucial role during woodchip gasification. Thus the kinetics for woodchip pyrolysis might have significant influence on gas composition.

From experimental data, the new woodchip pyrolysis could be written in the following equation:

$$Woodchip(CH_{1.64}O_{0.69}) \rightarrow 0.5Char + 0.087H_2 + 0.1CO + 0.063CO_2 + 0.035CH_4 + 0.09tar + 0.12H_2O \quad (37)$$

4.2 Model validation

The comparison of producer gas composition between experimental data and model (thermal-equilibrium and 3D CFD models) predictions is shown in **Figure 8**. It is shown that the model predictions are generally in good agreement with the experimental data: both the thermal-equilibrium and 3D models could predict the gas composition within 10% difference from the experimental data. It could also be found that with pyrolysis kinetics calculated from experimental data, the difference between experimental data and CFD simulation results decrease especially for H_2 production. This illustrated that pyrolysis plays an important role in gasification process and could greatly affect gas composition.

It is worth noting that compositions of CO and CH_4 are slightly over-predicted in CFD models. The possible reasons for this phenomenon are: a) In this simulation work, carbon is only considered in the forms of CO, CH_4, CO2 and char, while in real situations, other organic compositions such as ethane and ethylene exist; b) Some other CO and CH_4 related reactions are neglected in the simulation, such as methane reforming ($CH_4 + H_2O \leftrightarrow 3H_2 + CO$) and Fischer–Tropsch synthesis ($CO + H_2 \rightarrow hydrocarbon + H_2O$); c) Water shift reaction ($CO + H_2O \leftrightarrow CO_2 + H_2$) is an exothermic reaction. Because of the over-prediction of temperature in simulation, equilibrium favors reversed reaction, which leads to higher CO production.

The thermal equilibrium model was also validated with four groups of experiments: (a) pure woodchips gasification; (b) 10% sludge +90% woodchips; (c) 20% sludge +80% woodchips and (d) 33% sludge +67% woodchips, as shown in **Figure 9**. The details of experiments could be found in previous study (Ong et al., 2015). From the results, good agreements are found in terms of major gas compositions including CO, H_2 and CO_2 concentrations. This implied that the proposed model is valid and could be used to predict biomass gasification. Although methane is prediction is lower than experiments, it is worth noting that methane concentration is relatively low comparing with other major products. Thus this difference could be neglected.

The 3D CFD model was further validated by comparing the measured temperature at the bottom and top of the reduction bell to model predictions as shown in **Figure 10**. Generally, the modeled temperatures agree well with the experimental data. **Figure 10** also shows that the measured wall temperatures from the experiment are lower than the temperature inside the gasifier.

4.3 Model applications: Model-based gasifier operation and design

In this section, applications of the developed models were presented. The thermal-equilibrium model was applied to study the effects of air to biomass ratio on gas composition, LHV (lower heating value) and temperature, while the 3D model was applied to study the distribution of various physicochemical parameters inside the gasifier as follows. In addition, the effects of reduction bell dimension and heat loss mechanism

at the wall on the temperature distribution and syngas production were studied by the 3D CFD model.

4.3.1 Thermal-equilibrium model

Effect of sludge mixture ratio on gas composition and tar production is demonstrated in **Figure 11(a)**. Owing to the low higher heating value (HHV) of sludge (14.4-15.0 MJ/kg) compared with woodchip (17.0-18.2 MJ/kg), with the addition of sludge in the feedstock, both CO and H_2 concentration declined accordingly while tar production increased contrarily. It is probably due to the drop of temperature when 'bad' fuel, such as sludge, was fed into the system. This suggests that the addition quantity of low quality fuel as feedstock should be carefully controlled to reduce tar formation.

Equivalence ratio (ER), a key operation indicator, was varied from 0.25 to 0.4 to study its effect on gas composition and tar yield, as shown in **Figure 11(b)**. It is found that with increasing ER value, syngas (CO and H_2) concentration decreases, which lead to a lower quality gas product. This is because more air input intends to promote exothermic combustion reactions and thus the increase of temperature, which converts the syngas (CO and H_2) of high heating value to CO_2 and H_2O and thus decreases the heating value of the producer gas. It is noted that due to less air supply, lower operation temperature may lead to the formation of tar, a mixture of different compounds (e.g., cyclic hydrocarbons, aromatics and so on) of the dew point around 120 °C (around 400K)(Jordan and Akay, 2013), which would affect the quality of producer gas and thus is unwanted. Based on the thermal-equilibrium model, the optimal ER in terms of high quality of syngas production and low production of tar could be determined during practical applications.

4.3.2 3D CFD model

(1) Pressure and flow field distribution

The pressure, gas velocity, and velocity vector distribution throughout the whole gasifier are shown in **Figure 12**. **Figure 12i-(a)** shows that the pressure decreases along the axial direction from the top to the bottom of the gasifier. The highest pressure zones are located at the air inlet. Above the air inlets, the pressure distribution is uniform in both axial and radial directions. The lowest pressure zone is located at the outlet of the gasifier.

The pressure gradient indicates that the entering gas phase from the top will go through the combustion zone and further move into reduction bell, which is confirmed by the velocity vector distribution (**Figure 12i-(c)**). Since there is no pressure gradient around the area above the air inlets, no or little gas flow would be expected within the region. This is confirmed by **Figure 12i-(b)** which shows that the gas velocity above the air inlets zone is extremely low. The high gas velocity area is located at the top section of the reduction bell due to the small size of that section. The gas velocity decreases along the reduction bell from the top to bottom, corresponding to the increasing diameter of the reduction bell. Generally, the gas velocity near the wall is smaller than that near the center, which suggests the accumulation potential of solids close to the wall.

More details about the axial and radial velocity distributions are shown in **Figure 12**. The gas flows from the five air inlets interact with each other as well as the solid phase. Small vortex flows emerge around the gas inlet region. The major gas flow moves downwards and towards the reduction bell along the central line (**Figure 12ii-(b)**), while little gas moves upwards to the upper region of the air inlets (**Figure 12ii-(c)).** The flow field distribution suggests that the region above the air inlet will be an oxygen shortage zone and provides an environment for wood pyrolysis, as little entering oxygen would move upwards there. Meanwhile, the combustion zone will be located at or below the air nozzles, where plenty of oxygen is supplied.

(2) Temperature distribution

The temperature distributions (axial and radial) inside the gasifier are shown in **Figure 13**. The temperature is not distributed uniformly throughout the gasifier, due to the combined effect of irregular gasifier geometry and non-uniform flow behavior. The radial temperature distribution shows a V shape above the reduction bell while an inverted V shape inside the reduction bell. The high-temperature regions are located at the top of the reduction bell and along the tapered column under the air inlets. For the region above the air inlets, the temperature decreases upwards. The combustion occurs at or below the air inlets where the oxygen supply is adequate due to the downwards air as just shown in **Figure 12**. Hence, the heat release from the combustion leads to the high temperature in these regions. The heat transfer is associated with the gas phase motion (i.e. heat

convection), which results in a V-shaped distribution above the reduction bell and an inverted V-shaped distribution inside the reduction bell.

The radial temperature distributions at different heights of the gasifier show that the low-temperature regions are distributed at the center of the cross-section (i.e. central region) and the vicinity of the wall (i.e. surrounding region). The central low-temperature regions are resultant from the strong heat convection of gas phase, which is consistent with the above finding that the gas phase velocity of the central region is much higher than that of others. The surrounding low-temperature region is attributed to the fact that the contact area between the gas phase and fuel particles decreases near the wall due to the existence of the wall. The temperature distribution information is important for improving the performance of gasifiers. For example, upon the understanding of temperature distributions, heat-resistant materials could be specifically applied in the region of high temperature instead of all the regions, helping to reduce the cost but effectively protect the gasifier.

Gasification process usually goes through four continuous steps including drying, pyrolysis, combustion and reduction. Referring to the temperature profile, a rough division of four zones could be recognized. As shown in **Figure 7**, pyrolysis reaction starts around 250 to 300 °C. According to Ong's work (Ong et al., 2015), the temperature of pyrolysis zone could reach as high as 800 °C (1073 K) and the temperature of reduction zone start from 950 °C (1223 K). Based on these information and the gasifier structure (like air inlets positions and reduction bell), the boundaries of four zones could be estimated as shown in **Figure 13**. Noting that there is overlapping between different zones, divisions could not be exactly accurate. This division of four zones would give more detailed and intuitive understanding inside the reactor.

(3) Gas composition distribution

Gas composition is one of the most important indicators for the gasification process. The distributions of H_2, CO, CH_4 and CO_2 inside the gasifier is shown by **Figure 14**. Almost all of these gases are located at the lower portion of the gasifier, resulting in a conic-shaped interface between the lower gas-inclusive portion and upper gas-free portion. The gas distribution pattern is due to that: (1) the upper portion of the gasifier is occupied by the drying zone where chemical reactions rarely occur; (2) As mentioned in

the model development section, the formation of these gases starts from the pyrolysis zone. The gas phase velocity is higher around the central region than the surrounding (close to the wall) region (**Figure 12**), forming the conic interface. In addition, the V-shaped temperature distribution at the upper portion of the gasifier would also affect the gas distributions by controlling the chemical reactions. The amount of gas product is also demonstrated in **Figure 8** where good agreement is observed. Generally, the major composition is CO and H_2, which take up around 15-22% in different cases (with different pyrolysis kinetics). On the other hand, CO_2 takes up around 12% of total gas in both models and experiments, while CH_4 concentration is around 5-7% in the simulation. The reasons for the over-predictions of CH_4 and CO have been discussed in section 4.2.

(4) Char distribution

Char, a useful carbon-rich byproduct from gasification, serves a reactant in the gasification process especially in reduction zones for syngas production (Maneerung et al., 2016). On the other hand, it could also be transformed into activated carbon and used as an adsorbent material.

The char distribution inside the gasifier is shown in **Figure 15**. It is found that char is formed in pyrolysis, combustion, and reduction regions. Highest char fraction can be seen at the reduction bell region. This is because the combustion of char is inhibited in this region due to lack of oxygen.

4.3.3 Effects of reduction bell dimension

The reduction bell plays a significant role in the syngas production process. Using the developed 3D CFD model, a new gasifier design was proposed to study the effect of reduction bell size. The newly designed reduction bell is with a top of 0.155 m and a bottom of 0.254 m in diameter. The top and bottom of the original design have a diameter of 0.076 m and 0.152 m, respectively. The temperature and gas composition distributions inside the new gasifier are shown in **Figure 16**. Compared to the commercial design (**Figures 13-14**), different temperature and gas distribution profiles are observed (**Figure 16(a)-(b)**) for the new design. Instead of a V-shaped temperature distribution, a flat region at the bottom of V is obtained. In addition, the high-temperature regions are located near the air inlet regions rather than the tapered column. With a larger reduction

bell, the gas phase could pass through the top of reduction bell and bring the released heat from combustion zone to reduction zone more easily, which avoids the accumulation of heat at the tapered column. Therefore, the temperature value in the hottest region is much lower than that shown in **Figure 13**. It is also found that the temperature radial distribution at the top of reduction is more uniform and low-temperature zone at the central region can be hardly observed when compared to the commercial design. As shown in **Figure 16(b)**, the gas distribution profiles display a similar pattern to the temperature distribution, indicating that the gas distributions may be mainly affected by the temperature distribution that controls the chemical reactions inside the gasifier.

Quantitative comparison of temperature at the top and bottom of the reduction bell is shown in **Figure 17 (a)**. Both temperatures at the top and bottom of the reduction bell generally decrease when using larger reduction bell (new design), compared to the original design. Much lower temperature (~24%) at the bottom (gas outlet) of reduction bell is obtained for the new design. **Figure 17(b)** shows that the higher mole fractions of CO, H_2 and CH_4 are produced while the amount of CO_2 almost keeps the same, suggesting that the syngas production is enhanced using the newly designed gasifier. One of the possible reasons for the improved syngas is that due to the wider reduction throat, gas velocity decreases at in the reduction zones. As a result, residence time of materials in this zone where CO and H_2 are mainly produced extended.

4.3.4 Effect of air inlet velocity

In the work done by Ong and colleagues (2015), it was found that when air flow rate increased from 4 L/s to 7 L/s, gas composition was almost the same. Usually in a gasification system, when air input increases, syngas composition will drop because of more combustion reactions. Explanations for this strange phenomenon were not provided. In this section, the influences of air inlet velocity towards gasification are studied. In real operation of a downdraft gasifier, there is usually an auto-feeding system to maintain solid fraction. In this simulation, a constant solid fraction was assumed. **Table 6** shows the effects of air inlet velocity when it was changed from 1.54 m/s to 3.00 m/s. Gas compositions only change slightly which is consistent with experimental results. Also,

temperature increments of around 50 °C are found at both the outlet and the top of the reduction bell, following the same trend as experiment temperature profile.

Cold gas efficiency (CGE) is calculated based on the heating value ratio between produced gas and consumed woodchips, as defined in Equation (38).

$$CGE = \frac{Produced\ gas\ HHV \times Produced\ gas\ rate}{Feedstock\ HHV} \quad (38)$$

It is found that both cases have the same CGE of 63%, in good agreement with the reported value of 67% (Ong et al., 2015). The reason for few changes in gas composition with different air speed is that when more air goes into the reactor, combustion reactions are favored leading to a higher temperature and thus promoting all sorts of reactions including woodchip pyrolysis. When reaching steady state, the equivalence ratios between biomass consumption and air input for difference air input velocity are close, which leads to similar gas composition product.

4.3.5 Effect of operation environments

There are usually two operation environments for a gasification system, i.e. indoor and outdoor operation, respectively. Different scenarios may cause different mechanisms for heat loss of the system. The heat loss may mainly be dominated by natural convection when the machine is operated under indoor condition while forced convection may dominate the heat loss under outdoor operation. Therefore, three case studies considering heat loss of the gasifier under conditions of adiabatic (case 1), natural convection (case 2) and forced convection at wind speed of 1.5 m/s (case 3) were performed to investigate the effect of operation condition on the gas production. During experiment, outer wall temperature of the gasifier was measured at three different height locations. At each height, three sampling points were also used to get an average temperature reading. The average readings for three heights were 95.8 °C, 102.6 °C and 105.9 °C, from top to bottom respectively. To simplify the calculation, a uniform temperature of 100°C was assumed. The wind speed was also measure during experiment. The reading varied from 0.5 to 2.5 m/s. For simple calculation, 1.5m/s was used in case 3. The heat loss of each mechanism was calculated theoretically and coupled with the CFD model to perform the simulation. The equations and parameters used for calculating the heat loss are listed in **Table 7** and detailed values for different cases are listed in **Table 8**.

Table 8 shows that both natural and forced convection could reduce the temperature inside the reactor for around 40 °C at the reactor outlet, while gas compositions are almost the same in all three cases. It is probably because that the heat generated in the reactor by exothermal reactions is much bigger than the heat loss at boundary, making it negligible. This results show that the effects of heat loss are very small and adiabatic is a valid assumption when studying wall conditions. In addition, investigations of the effect of heat loss also suggest that indoor or outdoor operation of current gasification system will hardly affect the outcome of gas production.

5. Discussion

5.1 Insights into gasification based on modelling

In the previous study (Ong et al., 2015) it was found that blockage occurred during the gasification of 33 wt% sludge with 67 wt% woodchips (i.e. co-gasification), due to the formation of agglomerated blocks consisting of metallic iron and calcium carbonate. It was speculated that the high iron concentration in the feedstock was one of the main reasons for the blockage by the original study. The current CFD simulation results could provide an extra explanation to the speculation. As illustrated in **Figure 13**, the highest temperature is as high as 2000 K around the certain part of the combustion zone, which could easily melt and combine the metallic iron (melting point ~1500 K) (Swartzendruber, 1982) with other inorganic compounds. The V-shaped temperature distribution is formed above the reduction bell, and the low temperature regions are located around the centres of the cross-sections. The low temperature would solidify the melting mixture of metallic iron and inorganic compounds and form agglomerated blocks. Due to the small size of the reduction bell top, blockage will happen once the accumulated size of the agglomerated blocks is larger than that of the reduction bell. Benefitted from the prediction by the developed 3D CFD model, the simulation results indicates that this problem can potentially be solved by using larger reduction bell.

5.2 Comparison among thermal-equilibrium, 1D, and 3D models

The difference between the developed thermal-equilibrium and 3D models and existing 1D models is briefly commented. Thermal-equilibrium model could predict gas composition with limited input information such as feedstock composition and air rate. However, due to its natural limitations, this model can be applicable only when residence time of materials in the reactor is long. In addition, thermal equilibrium model is independent with reaction kinetics, which makes results less credible. Existing 1D kinetic models consider chemical kinetics and could distinguish the difference between feedstock and co-gasification agents. The co-gasification process can be studied and the optimum ratio between feedstock and co-gasification agents could be predicted by the 1D models. However, the boundaries of different zones are defined separately without overlapping, which is far from real situations. For both thermal-equilibrium model and 1D models, users could hardly obtain inside information of gasifiers. For the 3D CFD model, the multiphase flow model could be used to describe the behaviours of different phases associated with different chemical reactions and more details inside the reactor including gas composition profile and reaction zone division could be obtained, despite the complexity of the model would increase dramatically compared to thermal-equilibrium and 1D models.

6. Conclusions

In this study, a 3D CFD model together with a thermal-equilibrium model has been built and applied to study the downdraft gasifier. Model validation was conducted by comparing experimental data with model predictions in terms of gas composition and temperature, respectively, and generally a good agreement was found. The kinetic information for woodchip pyrolysis reaction was studied experimentally to further improve the CFD model. After using the new kinetics, the syngas compositions showed better fit with simulation. Thermal-equilibrium model was applied to study the effects of the air to biomass ratio on gas composition, LHV and temperature. Optimal conditions were suggested to maximize the syngas production and improve the quality of producer gas, respectively. The 3D model was further applied to study the distributions of various parameters (i.e. pressure, gas velocity, temperature, gas composition) inside the gasifier that are critical to the design of gasifier. The 3D CFD simulation showed that the

temperature and syngas concentration distributions were non-uniform in both axial and radial directions. The low-temperature regions were mostly located at the central and surrounding portions of gasifier. A rough division of four gasification zones was determined based on temperature profile. The studies on temperature distributions and effect of heat loss through wall helped to guide the application of heat resistant materials in gasifiers. To avoid potential problems related to temperature distributions, such as blockage, a larger reduction bell was preferred according to the CFD simulation results. Simulation results showed the newly designed gasifier with wider reduction bell could enhance syngas production. The thermal-equilibrium and 3D models could be used as a practical tool for the model-based designing of downdraft gasifiers to achieve cleaner energy production.

Acknowledgements

This research program is funded by the National Research Foundation (NRF), Prime Minister's Office, Singapore under its Campus for Research Excellence and Technological Enterprise (CREATE) program. Grant Number R-706-001-101-281, National University of Singapore. We also acknowledge the technical assistance by Avraham Uzi-Sorsky (Ben Gurion University) and Raunaq Bagchi (Imperial College London) during their research attachment at NUS.

Nomenclature

A	Pre-exponential factor, consistent units
C, H, N, O	Mass fractions of carbon, hydrogen, nitrogen and oxygen
C_p	Heat capacity (kJ/(kmol·K)).
d	Diameter of particles (m)
D	Diameter of reactor (m)
E_i	Activation energy of reaction i (kJ/mol)
e_{ps}	Coefficient of restitution
g	Gravitational acceleration (m/s^2)
$g_{0,ps}$	The radial distribution coefficient
Gr_L	Grashof number

$H_{f,i}^{0}$	Heat of formation of i (kJ/kmol)
HHV	Higher heating value (MJ/kg)
h_{pq}	Interphase enthalpy between the p^{th} and q^{th} phases
h'_{pq}	Volumetric heat transfer coefficient between the p^{th} and q^{th} phases
h_q	Specific enthalpy of the q^{th} phase
k	Conduction heat transfer coefficient (W/(m K))
K	Equilibrium constant
K_{ps}	Momentum exchange coefficient between the solid phase s and phase p.
K_{pg}	Momentum exchange coefficient between the gas phase g and phase p
L	Reactor height (m)
LHV	Low heating value (MJ/Nm^3)
m	Mole ratio between air and feedstock
m_o	Initial mass (g)
m_f	Final mass (g)
m_t	Transit mass (g)
M_i	The molecular weight of i, g/mol
$\dot{m}_{pq}$	Mass transfer from the phase p to phase q (kg/ (m^3 s))
n_i	Mole of composition i in the final product (mol)
Nu_D, Nu_p	Nusselt number
P	Fluid pressure (Pa)
Pr	Prandtl number
q	Heat flux (W)
Q_{pq}	Intensity of heat exchange between the p^{th} and q^{th} phases (W/m^2)
Q_{air}	The amount of heating energy to generate hot air (kJ/kmol)
$\vec{q}_q$	Heat flux (W/m^2)
Ra_L	Rayleigh number
Re, Re_D	Reynold number
S_q	Source term
t	Time (s)
T	Temperature of gasifier (K)

T_{air}	Temperature of air after preheating (K)
T_f	Film temperature (T)
T_m	Maximum reaction rate temperature (T)
T_o	Surrounding temperature (T)
T_s	Outer wall surface temperature (T)
T_bred	Temperature at the bottom of reduction bell (K)
T_tred	Temperature at the top of reduction bell (K)
$\vec{v}_q$	Velocity of phase q (m/s)
Y_i	Mass fraction of species i
α	Feedstock conversion
α_c	Carbon conversion factor
α_i	Volume fraction of phase i
β	Heating rate (K/min)
κ_q	Thermal conductivity of the q^{th} phase (W/(m·K))
ρ_i	Density (kg/m^3)
$\bar{\bar{\tau}}_g$	Viscous stress tensor
μ	Viscosity (kg/(m·s))

References

Ahmed, T.Y., Ahmad, M.M., Yusup, S., Inayat, A., Khan, Z., 2012. Mathematical and computational approaches for design of biomass gasification for hydrogen production: A review. Renewable and Sustainable Energy Reviews 16, 2304-2315.

Balat, H., Kırtay, E., 2010. Hydrogen from biomass–present scenario and future prospects. International Journal of Hydrogen Energy 35, 7416-7426.

Channiwala, S., Parikh, P., 2002. A unified correlation for estimating HHV of solid, liquid and gaseous fuels. Fuel 81, 1051-1063.

Chen, X.Z., Luo, Z.H., Yan, W.C., Lu, Y.H., Ng, I.S., 2011. Three‐dimensional CFD‐PBM coupled model of the temperature fields in fluidized‐bed polymerization reactors. AIChE Journal 57, 3351-3366.

Cheng, Y., Thow, Z., Wang, C.H., 2016. Biomass gasification with CO 2 in a fluidized bed. Powder Technology 296, 87-101.

Ephraim, A., Pozzobon, V., Louisnard, O., Minh, D.P., Nzihou, A., Sharrock, P., 2015. Simulation of biomass char gasification in a downdraft reactor for syngas production. AIChE Journal, 62, 1079-1091.

Florin, N., Harris, A., 2007. Hydrogen production from biomass. The Environmentalist 27, 207-215.

Gao, N., Li, A., 2008. Modeling and simulation of combined pyrolysis and reduction zone for a downdraft biomass gasifier. Energy Conversion and Management 49, 3483-3490.

Gerun, L., Paraschiv, M., Vijeu, R., Bellettre, J., Tazerout, M., Gøbel, B., Henriksen, U., 2008. Numerical investigation of the partial oxidation in a two-stage downdraft gasifier. Fuel 87, 1383-1393.

Gidaspow, D., 1994. Multiphase flow and fluidization: continuum and kinetic theory descriptions. Academic press.

Groppi, G., Tronconi, E., Forzatti, P., Berg, M., 2000. Mathematical modelling of catalytic combustors fuelled by gasified biomasses. Catalysis Today 59, 151-162.

Gunn, D., 1978. Transfer of heat or mass to particles in fixed and fluidised beds. International Journal of Heat and Mass Transfer 21, 467-476.

Iribarren, D., Susmozas, A., Petrakopoulou, F., Dufour, J., 2014. Environmental and exergetic evaluation of hydrogen production via lignocellulosic biomass gasification. Journal of cleaner production 69, 165-175.

Jarungthammachote, S., Dutta, A., 2007. Thermodynamic equilibrium model and second law analysis of a downdraft waste gasifier. Energy 32, 1660-1669.

Jordan, C.A., Akay, G., 2013. Effect of CaO on tar production and dew point depression during gasification of fuel cane bagasse in a novel downdraft gasifier. Fuel Processing Technology 106, 654-660.

Klimantos, P., Koukouzas, N., Katsiadakis, A., Kakaras, E., 2009. Air-blown biomass gasification combined cycles (BGCC): System analysis and economic assessment. Energy 34, 708-714.

Kumar, M., Ghoniem, A.F., 2011. Multiphysics simulations of entrained flow gasification. Part II: Constructing and validating the overall model. Energy & Fuels 26, 464-479.

Li, X., Grace, J., Lim, C., Watkinson, A., Chen, H., Kim, J., 2004. Biomass gasification in a circulating fluidized bed. Biomass and Bioenergy 26, 171-193.

Lim, Y.-i., Lee, U.-D., 2014. Quasi-equilibrium thermodynamic model with empirical equations for air–steam biomass gasification in fluidized-beds. Fuel Processing Technology 128, 199-210.

Maneerung, T., Liew, J., Dai, Y., Kawi, S., Chong, C., Wang, C.H., 2016. Activated carbon derived from carbon residue from biomass gasification and its application for dye adsorption: Kinetics, isotherms and thermodynamic studies. Bioresource Technology 200, 350-359.

Marklund, M., Tegman, R., Gebart, R., 2007. CFD modelling of black liquor gasification: Identification of important model parameters. Fuel 86, 1918-1926.

Melgar, A., Perez, J.F., Laget, H., Horillo, A., 2007. Thermochemical equilibrium modelling of a gasifying process. Energy Conversion and Management 48, 59-67.

Mohammed, I.Y., Abakr, Y.A., Hui, J.N.X., Alaba, P.A., Morris, K.I., Ibrahim, M.D., 2017. Recovery of clean energy precursors from Bambara groundnut waste via pyrolysis: Kinetics, products distribution and optimisation using response surface methodology. Journal of Cleaner Production 164, 1430-1445.

Moharamian, A., Soltani, S., Rosen, M.A., Mahmoudi, S., Morosuk, T., 2017. A comparative thermoeconomic evaluation of three biomass and biomass-natural gas fired combined cycles using organic Rankine cycles. Journal of Cleaner Production 161, 524-544.

Ong, Z., Cheng, Y., Maneerung, T., Yao, Z., Tong, Y.W., Wang, C.H., Dai, Y., 2015. Co‐gasification of woody biomass and sewage sludge in a fixed‐bed downdraft gasifier. AIChE Journal 61, 2508-2521 (2015)

Papadikis, K., Gu, S., Bridgwater, A., 2009. CFD modelling of the fast pyrolysis of biomass in fluidised bed reactors. Part B: heat, momentum and mass transport in bubbling fluidised beds. Chemical Engineering Science 64, 1036-1045.

Patra, T.K., Sheth, P.N., 2015. Biomass gasification models for downdraft gasifier: A state-of-the-art review. Renewable and Sustainable Energy Reviews 50, 583-593.

Pedroso, D.T., Aiello, R.C., Conti, L., Mascia, S., 2008. Biomass gasification on a new really tar free downdraft gasifier. Revista Ciências Exatas 11.

Ravikiran, A., Renganathan, T., Pushpavanam, S., Voolapalli, R.K., Cho, Y.S., 2011. Generalized analysis of gasifier performance using equilibrium modeling. Industrial & Engineering Chemistry Research 51, 1601-1611.

Rollinson, A.N., Karmakar, M.K., 2015. On the reactivity of various biomass species with CO 2 using a standardised methodology for fixed-bed gasification. Chemical Engineering Science 128, 82-91.

Ruiz, J., Juárez, M., Morales, M., Muñoz, P., Mendívil, M., 2013. Biomass gasification for electricity generation: review of current technology barriers. Renewable and Sustainable Energy Reviews 18, 174-183.

Sadaka, S.S., Ghaly, A., Sabbah, M., 2002. Two phase biomass air-steam gasification model for fluidized bed reactors: Part I—model development. Biomass and Bioenergy 22, 439-462.

Sharma, A.K., 2008a. Equilibrium and kinetic modeling of char reduction reactions in a downdraft biomass gasifier: A comparison. Solar Energy 82, 918-928.

Sharma, A.K., 2008b. Equilibrium modeling of global reduction reactions for a downdraft (biomass) gasifier. Energy Conversion and Management 49, 832-842.

Shen, Y., Tan, M.T.T., Chong, C., Xiao, W., Wang, C.H., 2017. An environmental friendly animal waste disposal process with ammonia recovery and energy production: Experimental study and economic analysis. Waste Management, 68, 636-645.

Sheth, P.N., Babu, B., 2009. Modeling and simulation of downdraft biomass gasifier, Proceedings of 2009 Annual Meeting of AIChE, Gaylord Opryland Hotel, Nashville, TN, USA.

Swartzendruber, L., 1982. The Fe (Iron) System. Journal of Phase Equilibria 3, 161-165.

Syamlal, M., 1987. The particle-particle drag term in a multiparticle model of fluidization. EG and G Washington Analytical Services Center, Inc., Morgantown, WV (USA).

van de Kaa, G., Kamp, L., Rezaei, J., 2017. Selection of biomass thermochemical conversion technology in the Netherlands: a Best Worst Method approach. Journal of Cleaner Production, 166, 32-39.

Wang, C.H., Zhao, D., Tsutsumi, A., You, S. 2017. Sustainable energy technologies for energy saving and carbon emission reduction", Applied Energy, 194, 223-224.

Wang, S., Lin, H., Ru, B., Dai, G., Wang, X., Xiao, G., Luo, Z., 2016. Kinetic modeling of biomass components pyrolysis using a sequential and coupling method. Fuel 185, 763-771.

Wang, Y., Kinoshita, C., 1993. Kinetic model of biomass gasification. Solar Energy 51, 19-25.

Wu, Y., Zhang, Q., Yang, W., Blasiak, W., 2013. Two-dimensional computational fluid dynamics simulation of biomass gasification in a downdraft fixed-bed gasifier with highly preheated air and steam. Energy & Fuels 27, 3274-3282.

Xue, Q., Heindel, T., Fox, R., 2011. A CFD model for biomass fast pyrolysis in fluidized-bed reactors. Chemical Engineering Science 66, 2440-2452.

You, S., Tong, H., Armin-Hoiland, J., Tong, Y.W., Wang, C.H., 2017b. Techno-economic and greenhouse gas savings assessment of decentralized biomass gasification for electrifying the rural areas of Indonesia. Applied Energy, 208, 495-510.

You, S., Ok, Y.S., Chen, S.S., Tsang, D.C., Kwon, E.E., Lee, J., Wang, C.H., 2017a. A critical review on sustainable biochar system through gasification: Energy and environmental applications. Bioresource Technology, 246, 242-253.

Zainal, Z., Ali, R., Lean, C., Seetharamu, K., 2001. Prediction of performance of a downdraft gasifier using equilibrium modeling for different biomass materials. Energy Conversion and Management 42, 1499-1515.

Zhang, Y., Zhao, Y., Gao, X., Li, B., Huang, J., 2015. Energy and exergy analyses of syngas produced from rice husk gasification in an entrained flow reactor. Journal of Cleaner Production 95, 273-280.

Table 1. Existing mathematical and CFD models (*i.e.* thermal-equilibrium, 1D and 3D models).

References	Category	Gasifier type	Remarks
Florin and Harris, 2007	thermal-equilibrium	NA	Hydrogen production prediction
Jarungthammachote and Dutta, 2007	thermal-equilibrium	Downdraft	Producer gas composition prediction
Zainal et al., 2001	thermal-equilibrium	Downdraft	Producer gas composition and calorific value prediction; effect of moisture content in feedstock
Melgar et al., 2007	thermal-equilibrium	Downdraft	Producer gas composition and reaction temperature prediction
Sheth and Babu, 2009	1D kinetic	Downdraft	Producer gas composition prediction
Ong et al., 2015	1 D kinetic	Downdraft	4 zones division; producer gas production
Gerun et al., 2008	2D CFD	Downdraft	2D axisymmetric model; oxidation zone only
Wu et al., 2013	2D CFD	Downdraft	2D slab geometry; highly preheated air and steam
Marklund et al., 2007	3D CFD	Entrained bed	Effects of model parameters
Fletcher et al., 1998	3D CFD	Entrained bed	Trajectories of biomass and char; measures to avoid slagging
Xue et al., 2011	3D CFD	Fluidized bed	Biomass pyrolysis
Papadikis et al., 2009	3D CFD	Fluidized bed	Biomass pyrolysis

Table 2. Heterogeneous Chemical Reactions.

Heterogeneous Reactions	Stoichiometric Chemical Equations	Rate Equations (kmol/(m^3 ▪s))	Reference
R1: Boudouard Reaction	$C + CO_2 \leftrightarrow 2CO$	$r_1 = 4.4T \exp\left(-\frac{1.62 \times 10^8}{RT}\right)[CO_2]^{0.6}$	Kumar and Ghoniem (2011)
R2: Char-Steam Reaction	$C + H_2O \leftrightarrow CO + H_2$	$r_2 = 1.33T\ exp\left(-\frac{1.47 \times 10^8}{RT}\right)[H_2O]^{0.6}$	Kumar and Ghoniem (2011)
R3: Partial Oxidation	$C + 0.5O_2 \rightarrow CO$	$r_3 = 2.3Texp\left(-\frac{9.23 \times 10^7}{RT}\right)[O_2]^{0.4}$	Kumar and Ghoniem (2011)
R4: Methanation Reaction	$C + 2H_2 \leftrightarrow CH_4$	$r_4 = 4.189 \times 10^{-3}\ \exp\left(\frac{-1.92 \times 10^7{}_4}{RT}\right)P_{H_2}^2$	Wang and Kinoshita (1993)
R5: Pyrolysis	$Dried\ wood \rightarrow 2\ char + 0.39\ CO_2 + 0.42\ CO + 0.7\ H_2 + 0.22\ CH_4 + 0.15\ H_2O + 0.84\ tar$	$r_5 = 10^{4.03} \exp\left(-\frac{7.78 \times 10^7}{RT}\right)[wood]]$	Cheng et al. (2016)

Table 3. Homogeneous Chemical Reactions.

Homogeneous Reactions	**Stoichiometric Chemical Equations**	**Rate Equations (kmol/(m^3 ▪s))**	**Reference**
R6: Oxidation of CO	$CO + 0.5O_2 \rightarrow CO_2$	$r_7 = 3.98 \times 10^{14} \exp\left(-\frac{1.67 \times 10^8}{RT}\right)[CO][O_2]^{0.25}[H_2O]^{0.5}$	Groppi et al. (2000)
R7: Oxidation of H_2	$H_2 + 0.5O_2 \rightarrow H_2O$	$r_8 = 2.196 \times 10^{13} \exp\left(-\frac{1.09 \times 10^8}{RT}\right)[H_2][O_2]$	Groppi et al. (2000)
R8: Steam-Reforming Reaction	$CH_4 + 0.5O_2 \rightarrow CO + 2H_2$	$r_9 = 4.4 \times 10^{11} \exp\left(-\frac{2.02 \times 10^8}{RT}\right)[CH_4]^{0.5}[O_2]^{1.25}$	Kumar and Ghoniem (2011)
R9: Water Gas Shift Reaction	$CO + H_2O \leftrightarrow CO_2 + H_2$	$r_{10} = 2.78 \times 10^6 \exp\left(-\frac{1.26 \times 10^7}{RT}\right)\left([CO][H_2O] - \frac{[CO_2][H_2]}{K_p(T)}\right)$ $K_p(T) = 0.0265 \exp\left(\frac{4.55 \times 10^7}{RT}\right)$	Wu et al. (2013)
R10: Tar Cracking	$Tar \rightarrow 0.30CO_2 + 2.43CO + H_2 + 0.67CH_4$	$r_{11} = 2.08 \times 10^3 \exp\left(-\frac{6.63 \times 10^7}{RT}\right)[tar]$	Cheng et al. (2016)

Table 4. Simulation parameters and conditions.

Physical properties	
Woodchip density	602 kg/m^3
Woodchip particle diameter	0.04 m
Char density	2000 kg/m^3
Char particle size	0.02 m
Gas phase	mixture
Boundary and operating conditions	
Wall	No-slip
Initial volume fraction of packed biomass	0.6
Velocity of air inlet	1.54 m/s
Temperature of preheated air	500 K
Biomass feed rate	10 kg/h
Operating pressure	1 atm
Gravidity	9.81 m^2/s
Time step	10^{-7} s
Iterations	20

Table 5. Elemental analysis result for cone and quartering method.

Group	Sub-group	C (wt%)	H (wt%)	N (wt%)	S (wt%)
A	1	44.24	6.05	<0.50	<0.50
	2	45.94	6.03	<0.50	<0.50
	3	45.37	5.76	<0.50	<0.50
	Average	45.18±0.86	5.95±0.16		
B	1	46.82	5.84	<0.50	<0.50
	2	46.87	5.79	<0.50	<0.50
	3	42.65	6.01	<0.50	<0.50
	Average	45.45±2.42	5.88±0.11		
C	1	46.93	5.59	<0.50	<0.50
	2	46.93	5.57	<0.50	<0.50
	3	42.84	5.93	<0.50	<0.50
	Average	45.57±2.36	5.7±0.20		
D	1	42.96	5.63	<0.50	<0.50
	2	44.34	5.89	<0.50	<0.50
	3	45.68	5.68	<0.50	<0.50
	Average	44.33±1.36	5.73±0.14		

Table 6. Effects of air inlet velocity (Experimental data from Ong et al., 2015)

Air inlet velocity (m/s)	1.54		3.00	
Average temperature at reduction bell (K)	1689.17		1735.00	
Average temperature at outlet (K)	1222.06		1278.84	
Gas composition (%)	Experiment	CFD simulation	Experiment	CFD simulation
CO	16.0	20.1	16.5	19.8
H_2	17.6	17.5	17.4	17.2
CO_2	12.7	12.6	12.3	12.8

Table 7. The parameters and equations used for theoretical calculation of heat loss.

Forced convection	
Heat flux (w/m^2)	$\frac{q}{A} = Nu_D \frac{k}{L}(T_s - T_o)$
Nusselt number	$Nu_D = 0.193 Re_D^{0.618} Pr^{1/3}$ $(4000 < Re_D < 40000)$
Air velocity	1.5 m/s
Surface temperature	373 K
Air temperature	300 K
Natural convection	
Heat flux (w/m^2)	$\frac{q}{A} = Nu_L \frac{k}{L}(T_s - T_o)$
Nusselt number	$Nu_L = \left\{ 0.825 + \frac{0.387 Ra_L^{1/6}}{[1 + \left(\frac{0.492}{Pr}\right)^{9/16}]^{8/27}} \right\}^2$
Rayleigh number	$Ra_L = Gr_L \times Pr$
Film temperature (fluid properties evaluated at T_f)	$T_f = \frac{T_s + T_o}{2}$
Surface temperature	373 K
Air temperature	300 K

Table 8. Effects of heat loss in different cases.

Case number	1	2	3
Boundary conditions	Adiabatic	Natural convection	Forced convection (1.5 m/s)
Heat loss q/A (W/m^2)	0	409.1	601.9
Temperature at reduction bell (K)	1689.17	1677.08	1677.06
Temperature at outlet (K)	1222.06	1186.08	1186.06
CO % at outlet	15.3	15.3	15.4
H_2 % at outlet	25.4	25.4	25.4
CH_4 % at outlet	8	8	8

Figure

Figure 1. Simplified gasification process for thermal-equilibrium modeling.

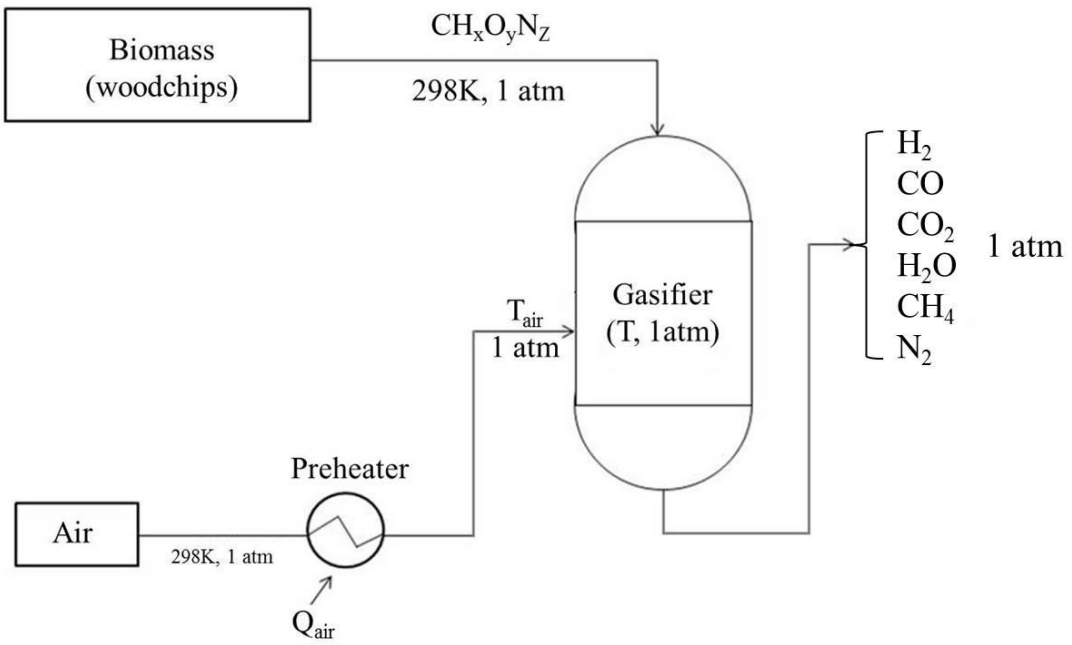

Figure 2. The physical model and the grid of gasifier for CFD simulation.

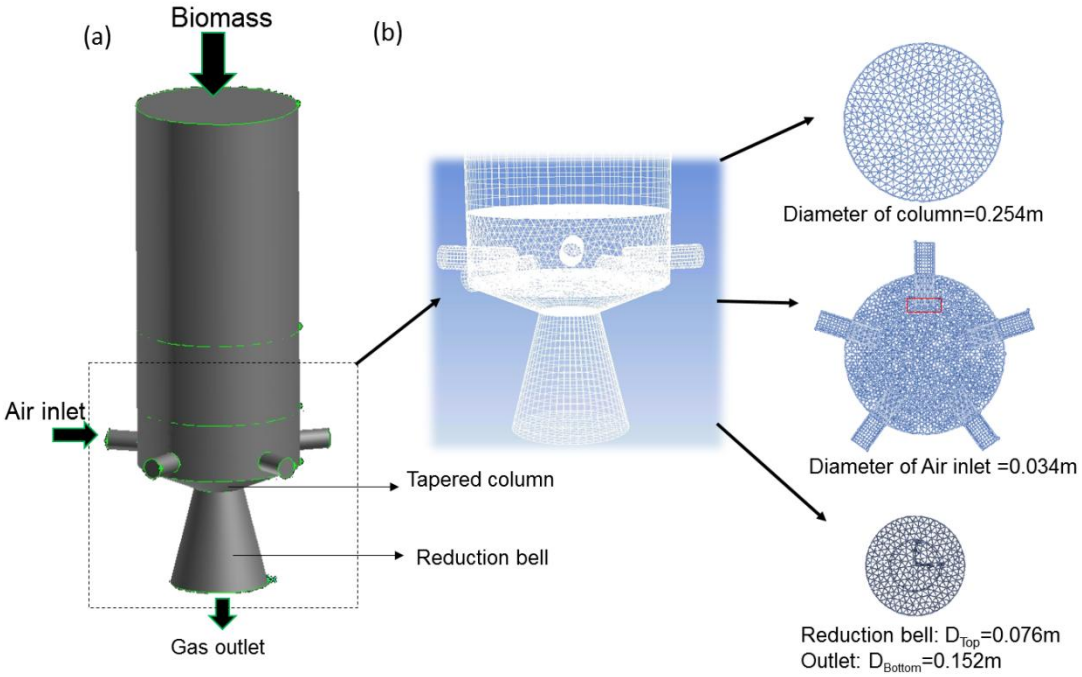

Figure 3. CFD simulation flow chart.

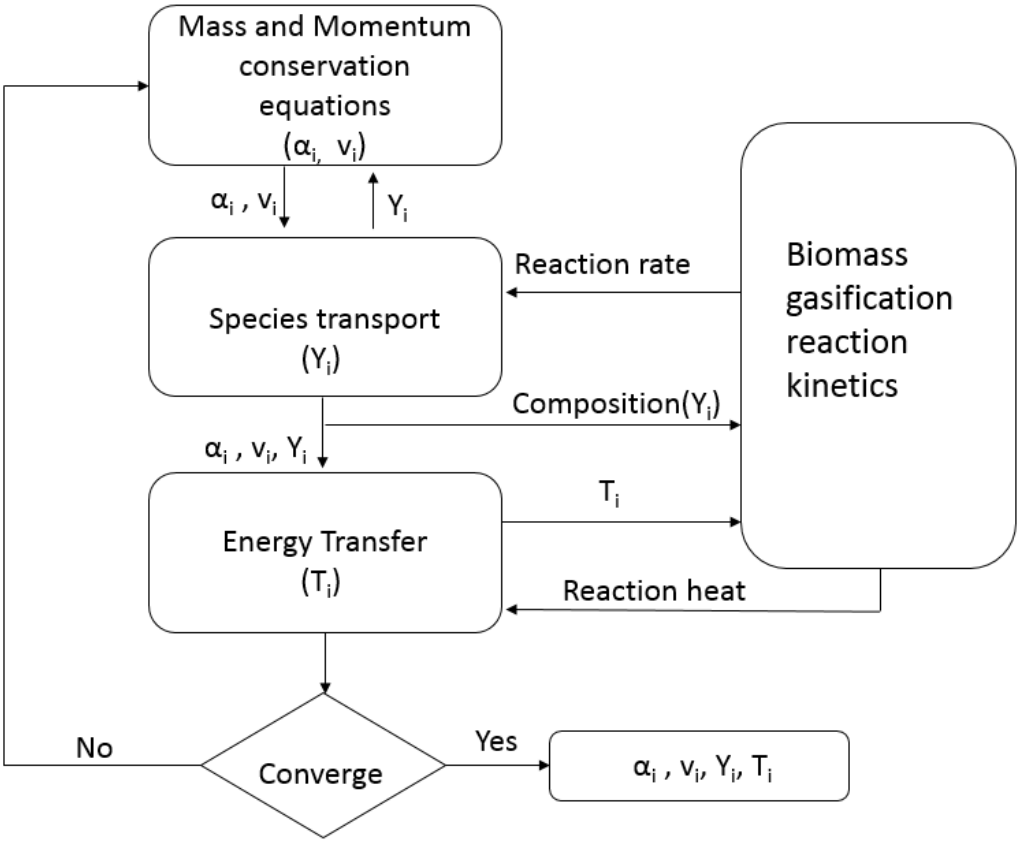

Figure 4. Schematic of the gasifier unit.

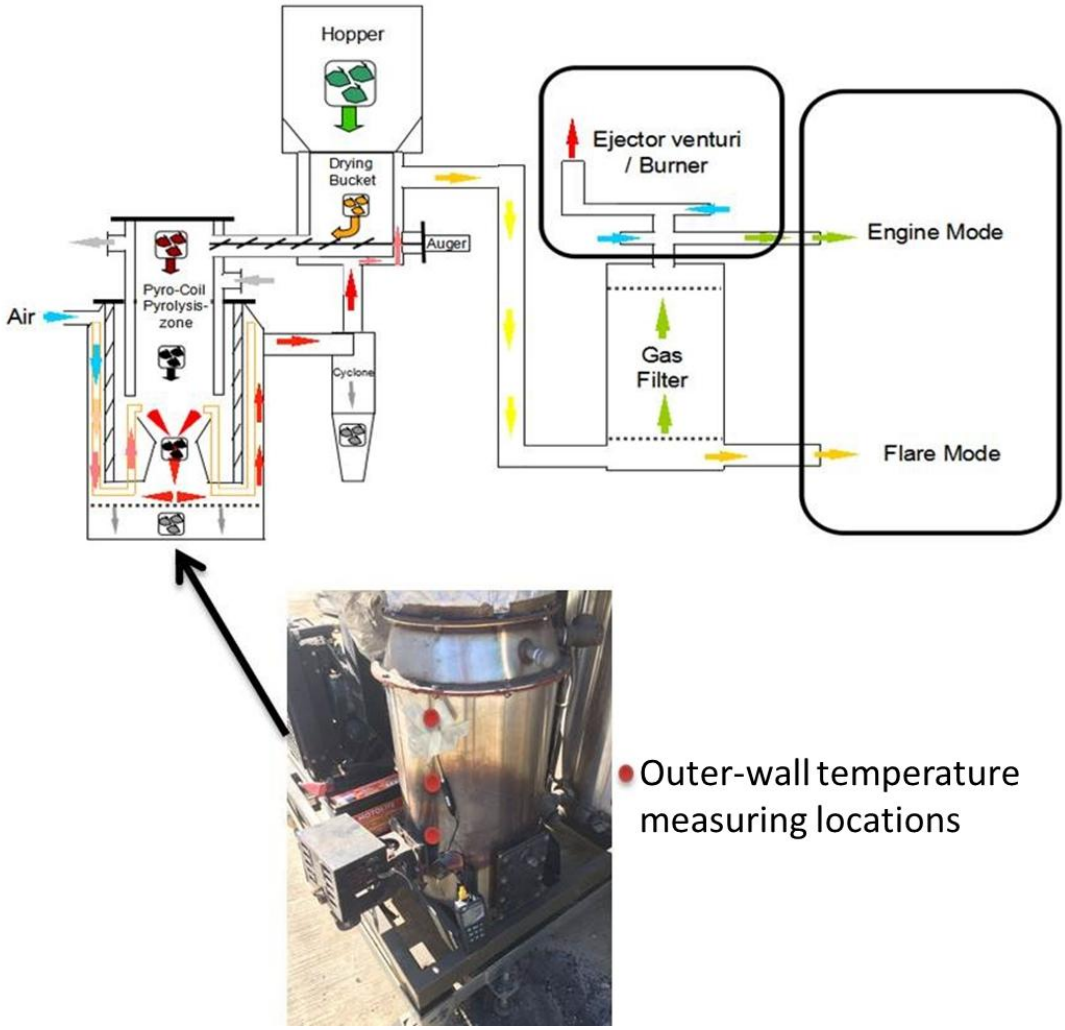

Figure 5. Scheme diagram of cone and quartering method for biomass sampling. (a: heap a cone; b: quarter the cone; c: choose opposite sub-samples to heap a new cone; d: quarter the cone; e final samples)

Figure 6. Scheme diagram of the lab-scale gasifier.

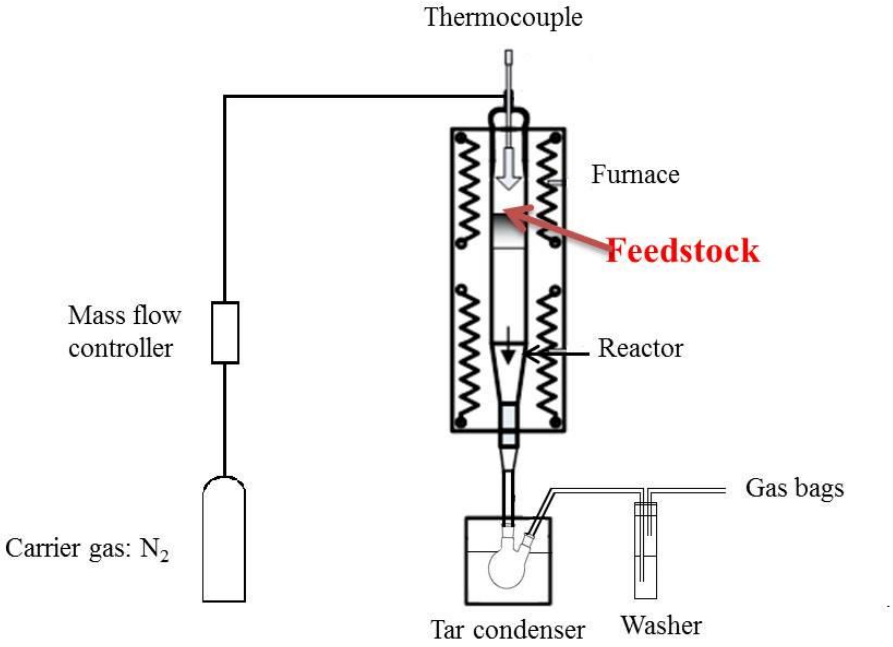

Figure 7. Experimental study of woodchip pyrolysis kinetics.

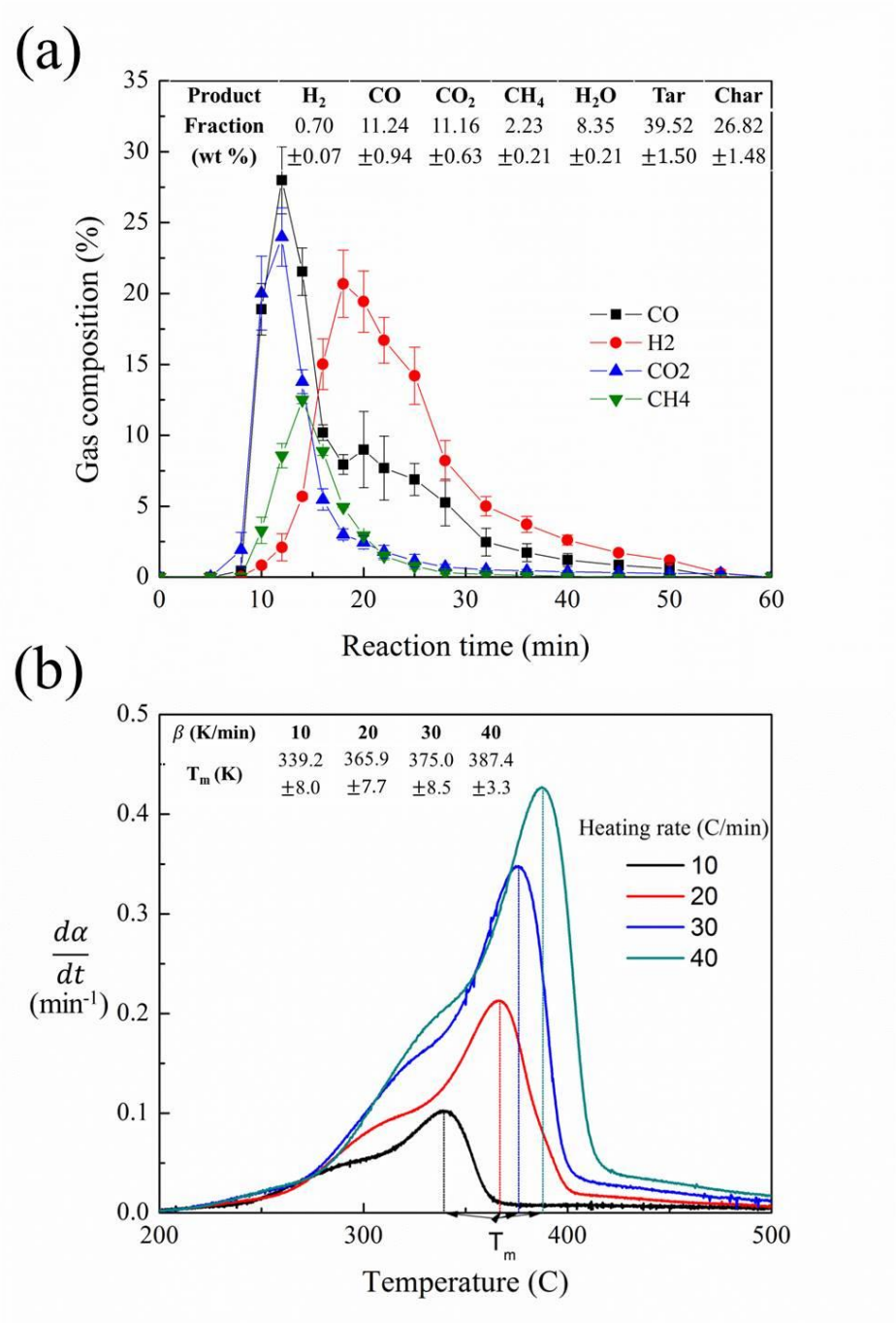

Figure 8. Comparison of the gas composition between CFD simulation and experimental results.

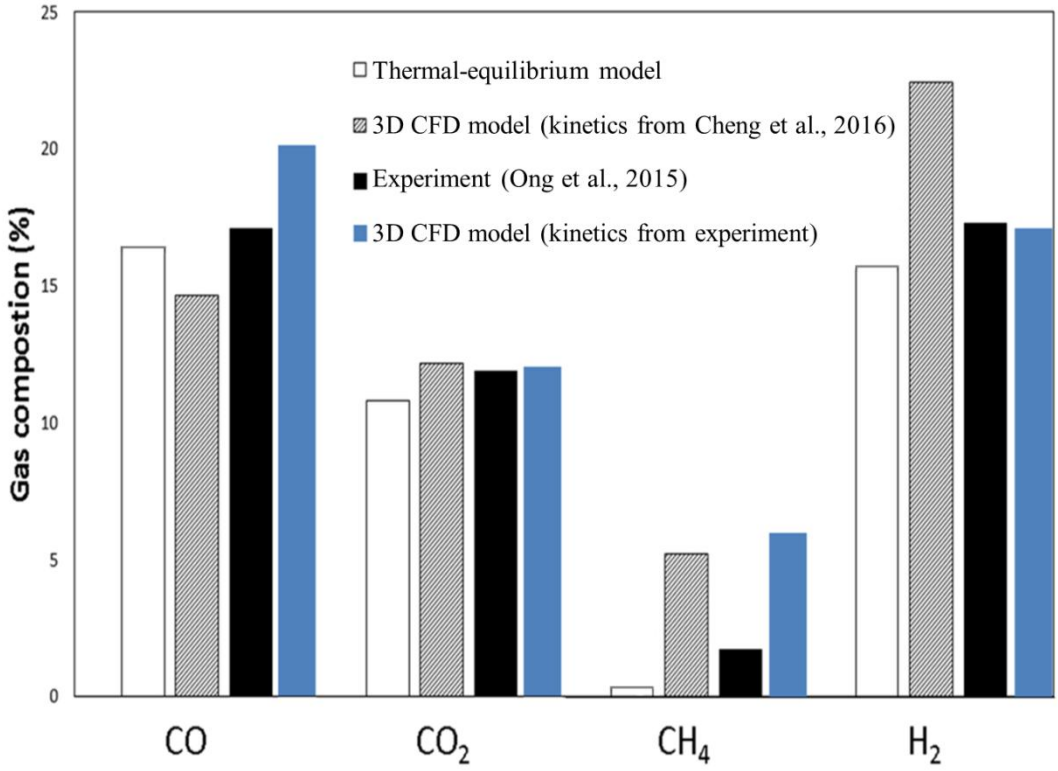

Figure 9. Thermo-equilibrium model validation: (a) pure woodchips; (b) 10% sludge +90% woodchips; (c) 20% sludge +80% woodchips; (d) 33% sludge +67% woodchips. (Experimental data from Ong et al., 2015)

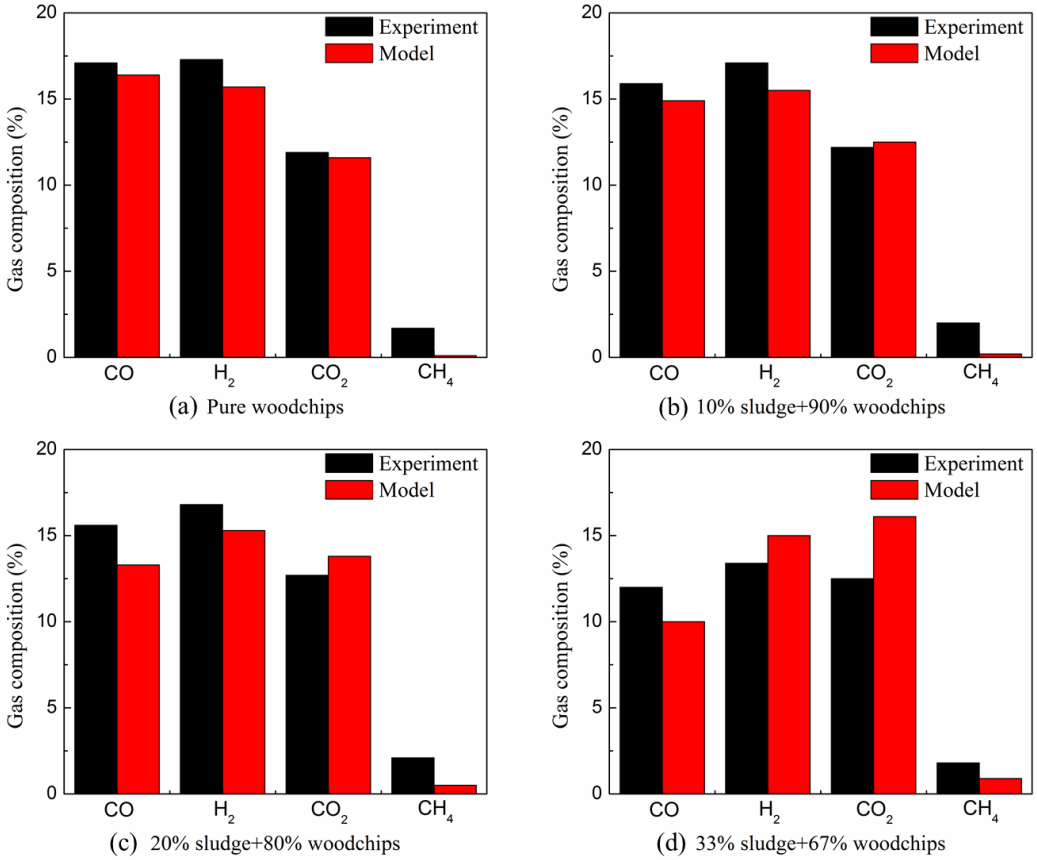

Figure 10. Comparison of the temperature between CFD simulation and experimental results.

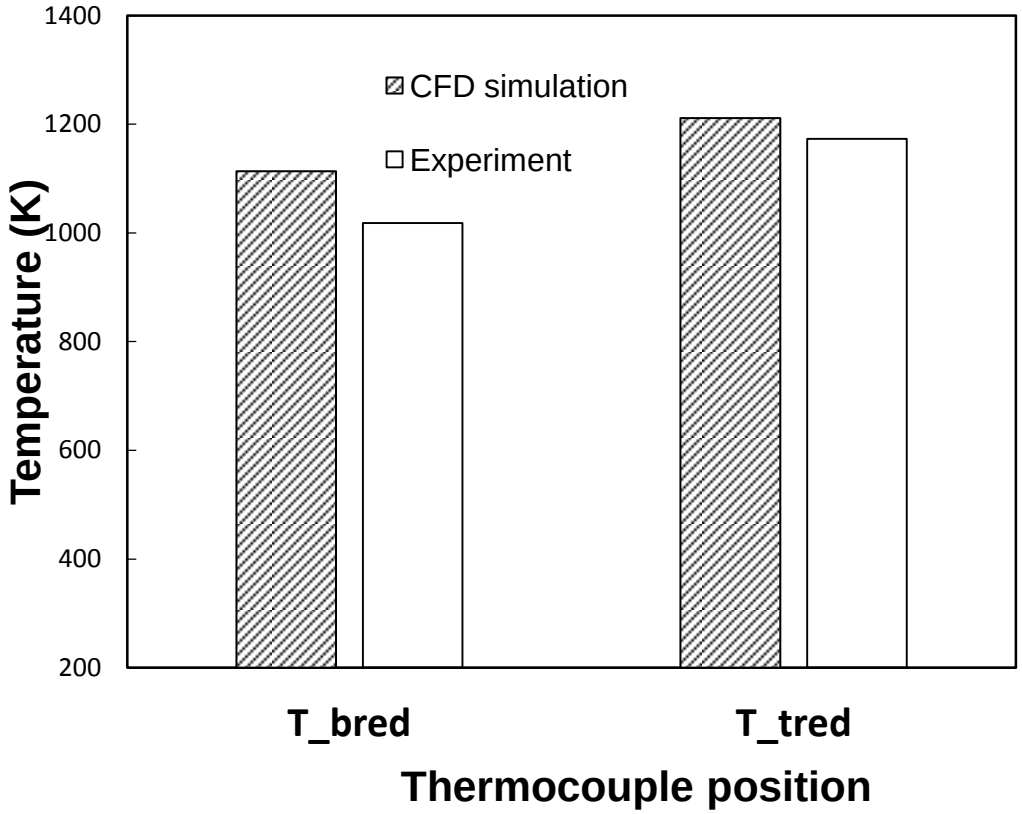

Figure 11. Effects of (a) sludge mixture ratio and (b) equivalence ratio on gas composition and tar production

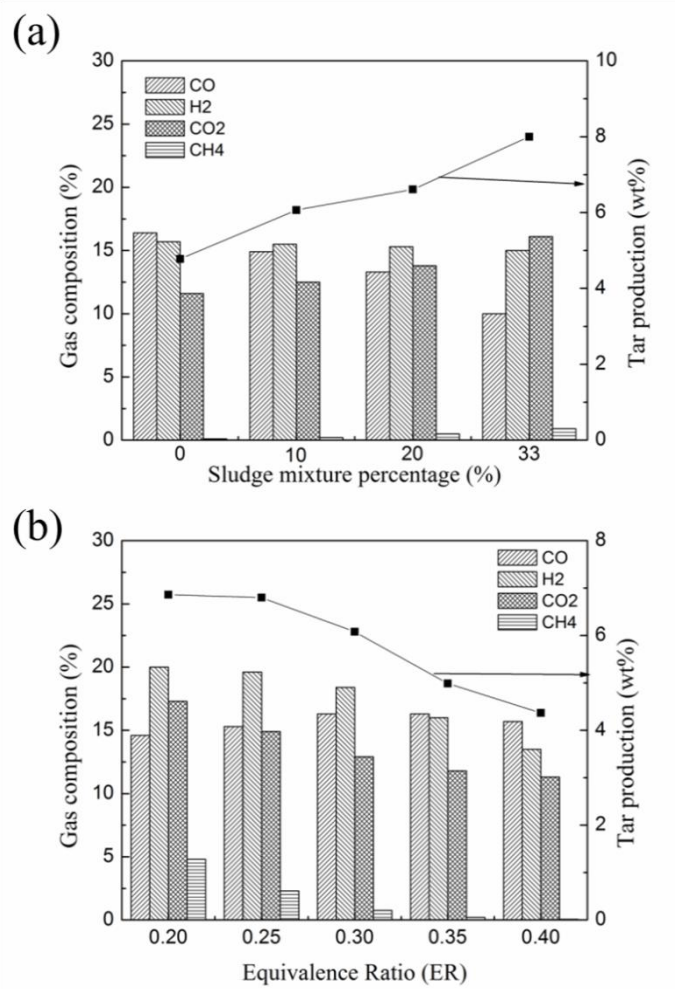

Figure 12. i: Pressure, velocity and velocity vector distributions inside the gasifier. ii: Axial and radial velocity vector distributions.

i

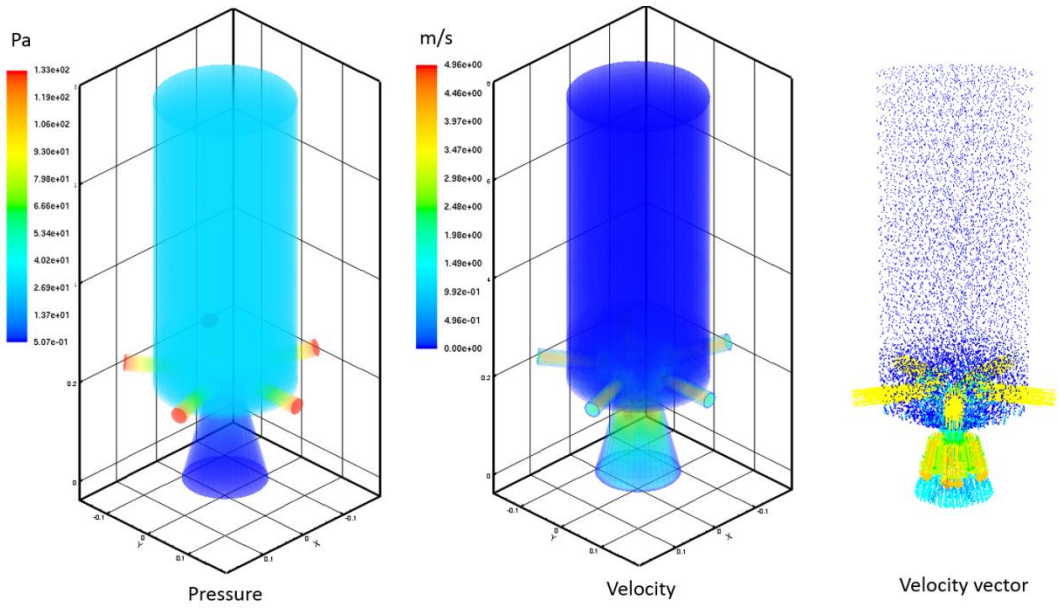

ii

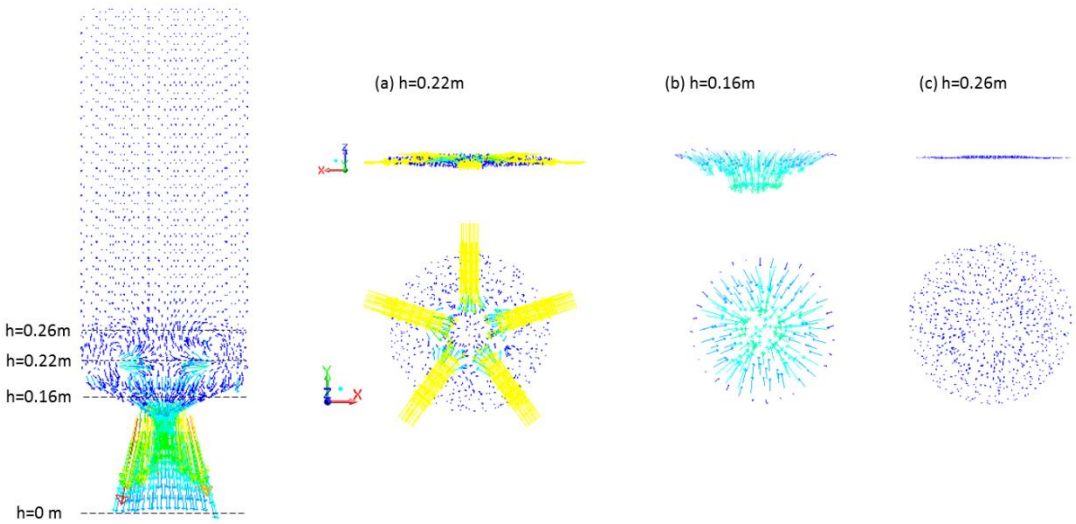

Figure 13. Temperature profile inside the gasifier.

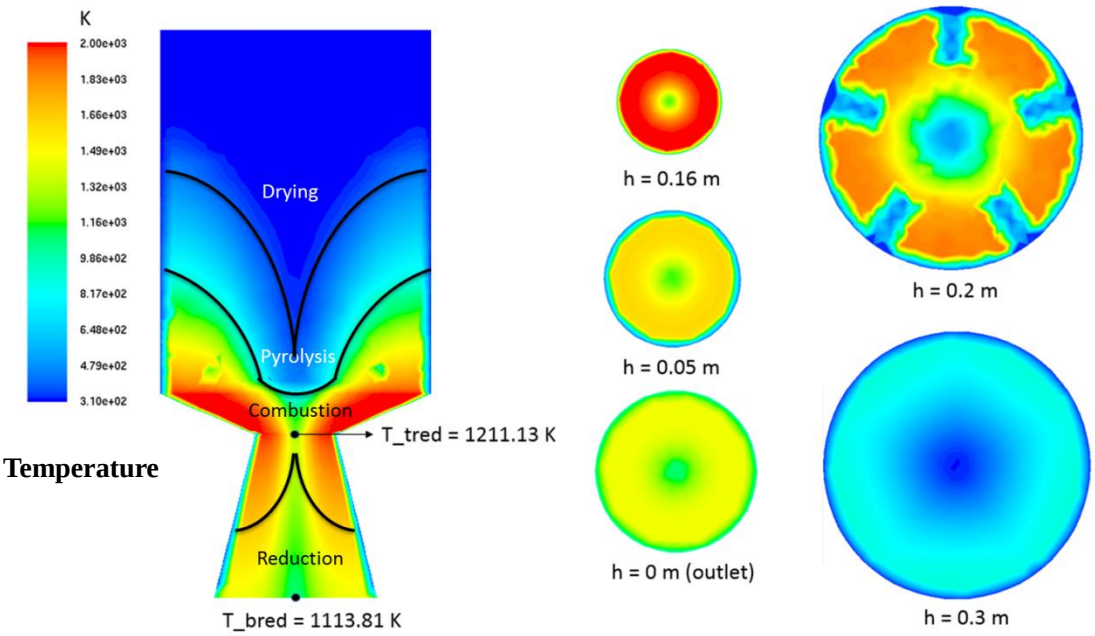

Figure 14. Gas composition distributions inside the gasifier.

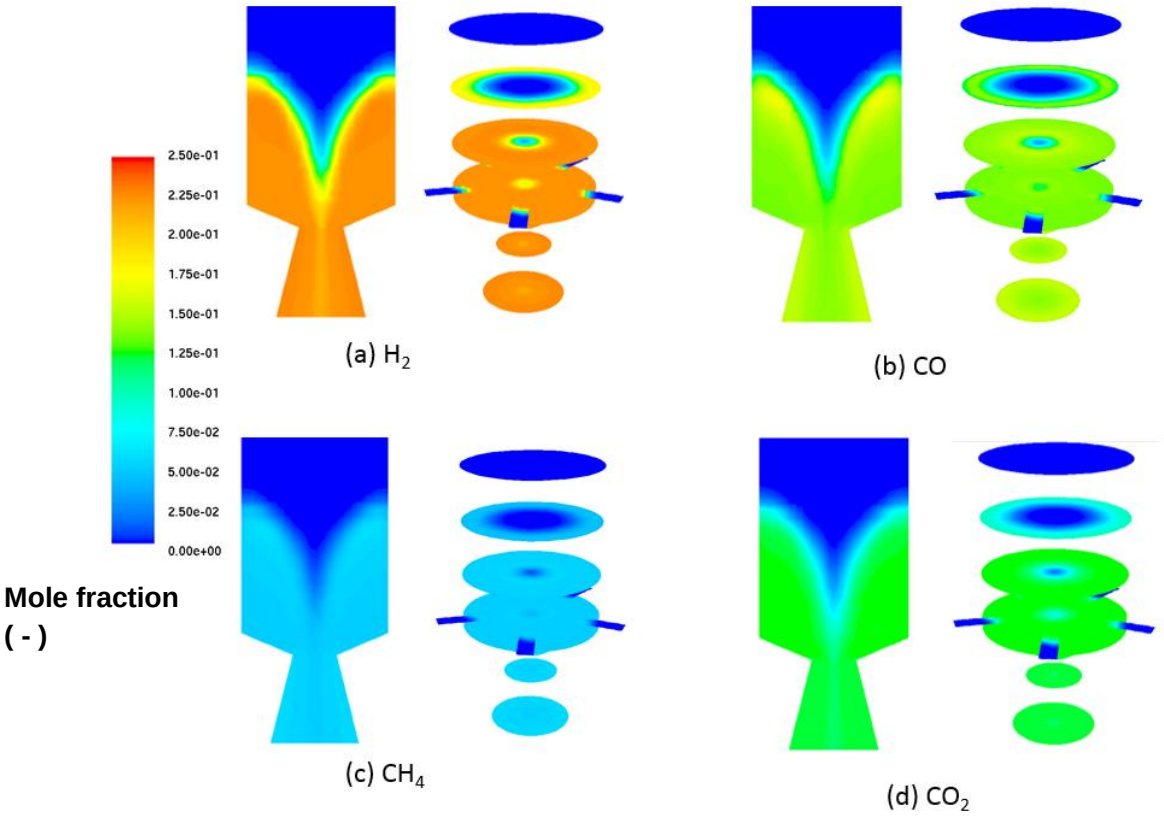

Figure 15. Char distribution inside the gasifier.

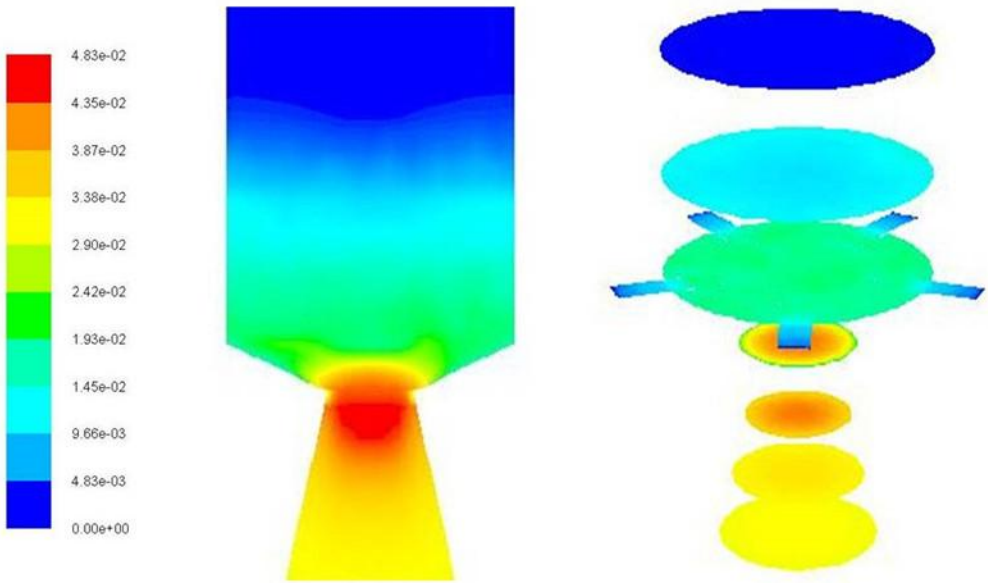

Figure 16. Temperature and syngas composition distributions inside the gasifier with the proposed reduction bell size.

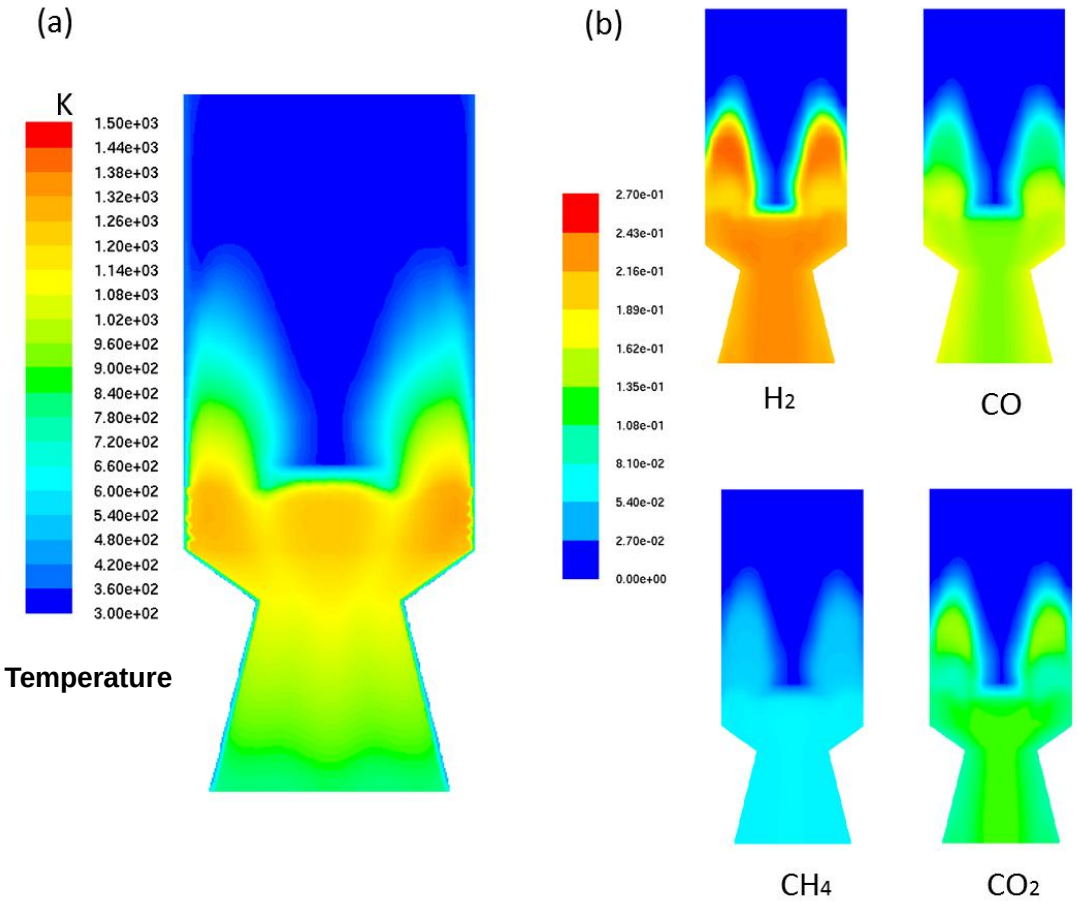

Figure 17. Comparison of temperature and syngas composition between the cases of different reduction bell sizes. (a) Temperature at the top and bottom of the reduction bell, (b) Syngas composition at the outlet of reduction bell.